PAPER

Modeling the vertical growth of van der Waals stacked 2D materials using the diffuse domain method

To cite this article: Zhenlin Guo et al 2020 Modelling Simul. Mater. Sci. Eng. 28 025002

View the <u>article online</u> for updates and enhancements.



IOP ebooks™

Bringing together innovative digital publishing with leading authors from the global scientific community.

Start exploring the collection-download the first chapter of every title for free.

Modeling the vertical growth of van der Waals stacked 2D materials using the diffuse domain method

Zhenlin Guo¹, Christopher Price², Vivek B Shenoy^{2,3,4} and John Lowengrub^{1,5}

E-mail: lowengrb@math.uci.edu

Received 8 October 2019, revised 20 November 2019 Accepted for publication 4 December 2019 Published 13 January 2020



Abstract

Vertically-stacked monolayers of graphene and other atomically-thin 2D materials have attracted considerable research interest because of their potential in fabricating materials with specifically-designed properties. Chemical vapor deposition has proved to be an efficient and scalable fabrication method. However, a lack of mechanistic understanding has hampered efforts to control the fabrication process beyond empirical trial-and-error approaches. In this paper, we develop a general multiscale Burton-Cabrera-Frank type model of the vertical growth of 2D materials to predict the necessary growth conditions for vertical versus in-plane (monolayer) growth of arbitrarilyshaped layers. This extends previous work where we developed such a model assuming the layers were fully-faceted (Ye et al 2017 ACS Nano 11 12780–8). To solve the model numerically, we reformulate the system using the phasefield/diffuse domain method that enables the equations to be solved in a fixed regular domain. We use a second-order accurate, adaptive finite-difference/ nonlinear multigrid algorithm to discretize and solve the discrete system. We investigate the effect of parameters, including the van der Waals interaction energies between the layers, the kinetic attachment rates, the edge-energies and the deposition flux, on layer growth and morphologies. While the

¹ Department of Mathematics, University of California, Irvine, CA 92697-3875, United States of America

² Department of Materials Science and Engineering, University of Pennsylvania, Philadelphia, PA 19104-6272, United States of America

³ Department of Mechanical Engineering & Applied Mechanics, University of Pennsylvania, Philadelphia, PA 19104-6272, United States of America

⁴ Bioengineering, University of Pennsylvania, Philadelphia, PA 19104-6272, United States of America

⁵ Department of Biomedical Engineering, University of California, Irvine, CA 92697-3875, United States of America

conditions that favor vertical growth generally follow an analytic thermodynamic criterion we derived for circular layers, the layer boundaries may develop significant curvature during growth, consistent with experimental observations. Our approach provides a mechanistic framework for controlling and optimizing the growth multilayered 2D materials.

Keywords: graphene, chemical vapor deposition, multiscale models, freeboundary problems, diffuse interface methods

(Some figures may appear in colour only in the online journal)

1. Introduction

Two-dimensional (2D) materials including graphene and transition metal dichalcogenides (TMDs) have garnered unprecedented interest in pursuit of unique electronic, optical, mechanical, and thermal properties [1–5]. Compared to homogeneous monolayers, multilayered heterostructures contain many more degrees of freedom and thus can be ideal platforms for electronic structure engineering of atomically thin 2D semiconducting materials for novel applications. A key challenge in the realization of vertically integrated 2D layers is their synthesis [1, 6, 7]. Chemical vapor deposition (CVD) has proved to be an efficient and scalable method to grow monolayer 2D materials on a variety of metal substrates [8–11]. CVD, however, is a complex process that contains many parameters that influence growth. For example, the growth temperature and the deposition flux have been found to be critical parameters for switching from in-plane (monolayer) to verticallystacked multilayer growth. In WS₂/MoS₂ heterostructures on SiO₂/Si substrates, high temperatures favor the growth of vertically-stacked multilayers while low temperatures favor monolayer growth [8]. In graphene, a lower deposition flux (e.g. higher concentrations of H₂ in the gas) also tends to favor multilayer growth [12, 13]. Determining proper growth parameters is clearly a multivariable problem that until recently was tackled using empirical trial-and-error approaches.

In recent work, we developed a multiscale model of the growth of vertically-stacked 2D materials on a substrate using CVD [14]. The model, which is of Burton–Cabrera–Frank (BCF) type [15], accounts for attachment and diffusion of adatoms, van der Waals (vdW) interactions between the layers and the substrate, and edge energies of the layers. To simplify the system, the layers were assumed to be fully-faceted and so their shapes were constrained to be equilateral polygons (e.g. triangles and hexagons). This work predicted the thermodynamic requirements for growth of vertically-stacked faceted layers. The vdW-BCF model predictions on monolayer versus multilayer morphologies were validated by comparison with a variety of CVD-synthesized MX_2 (M = Mo, W; X = S, Se, Te) single-species samples grown under conditions of varying temperature and precursor flux.

However, as seen in the experiments in [10, 14] and in other references, the layers need not to be faceted and can develop significant, and even negative, curvatures. Because the layer morphologies influence growth and the material properties, it is important to accurately predict the layer shapes as well. In this paper, we extend the vdW-BCF model in [14] to account for arbitrary layer shapes. The resulting system is a highly nonlinear free boundary problem. We analyze the model and derive an analytic thermodynamic criterion for vertical growth assuming the layers are circular. To simulate the model when the layer geometries are

unconstrained, we develop a second-order accurate phase-field/diffusion-domain method (DDM) that enables us to simulate the system by solving a reformulated system (vdW-BCF-DDM equations) in a fixed regular domain.

The diffuse-domain, or smoothed boundary, method is an attractive approach for solving partial differential equations in complex geometries because of its simplicity and flexibility. In this method the complex geometry is embedded into a larger, regular domain. The original PDE is reformulated using a smoothed characteristic function of the complex domain and source terms are introduced to approximate the boundary conditions. An advantage of this approach is that the reformulated equations can be solved by standard numerical techniques without requiring body-fitted meshes, additional interfacial meshes or special stencils and the same solver can be used for any geometry. The diffuse-domain method (DDM) was introduced in [16] to solve diffusion equations with Neumann (noflux) boundary conditions, to PDEs with Robin and Dirichlet boundary conditions in [17] and to cases in which bulk and surface equations are coupled [18]. Later, in [19] and [20] alternate derivations of diffuse-domain methods for such problems were presented. In [21] a matched asymptotic analysis for general DDMs with Neumann and Robin boundary conditions showed that for certain choices of the source terms, the DDMs were secondorder accurate in ϵ and in the grid size h in both the L^2 and the L^{∞} norms, taking $\epsilon \propto h$, see the recent paper [22] for a rigorous proof.

In [23], a DDM was proposed to solve a BCF model of epitaxial growth of thin, crystalline films that combined a DDM reformulation of the adatom diffusion equations together with a Cahn–Hilliard-type equation to model the dynamics of the films. This approach considered only isotropic edge energies and kinetic coefficients and did not consider vdW interactions. Further, the DDM used in [23] did not use a second-order accurate formulation and thus was only first order accurate in ϵ (and h assuming $\epsilon \propto h$).

Here, we combine and extend the approaches from [21, 23] to develop a second-order accurate adaptive finite-difference/nonlinear multigrid method to discretize and solve the vdW-BCF-DDM equations numerically. We investigate the effect of parameters, including vdW interaction energies between the layers, kinetic attachment rates, edge-energies and deposition flux, on layer growth and morphologies. While the conditions that favor vertical growth generally follow the thermodynamic criterion we derived for circular layers, the layer boundaries may develop significant curvature during growth, consistent with experimental observations, that can also influence the growth kinetics.

The outline of the paper is as follows. In section 2, we present and analyze the vdW-BCF model for arbitrary layer shapes. In section 3 we present the phase-field/DDM reformulation of the vdW-BCF model and briefly describe the numerical methods used. In section 4, we present numerical simulation studies and in section 5 we present conclusions and discuss future work. Additional details are provided in the appendices.

2. The vdW-BCF model for the growth of vertically-stacked multilayers

Let Ω_0 denote the substrate, Ω_1 denote a layer of atomic height 1 and Ω_2 be a layer of atomic height 2 with boundaries Γ_0 , Γ_1 and Γ_2 , respectively. See the diagrams in figures E1 and E3 (left column). The system free energy is taken to be:

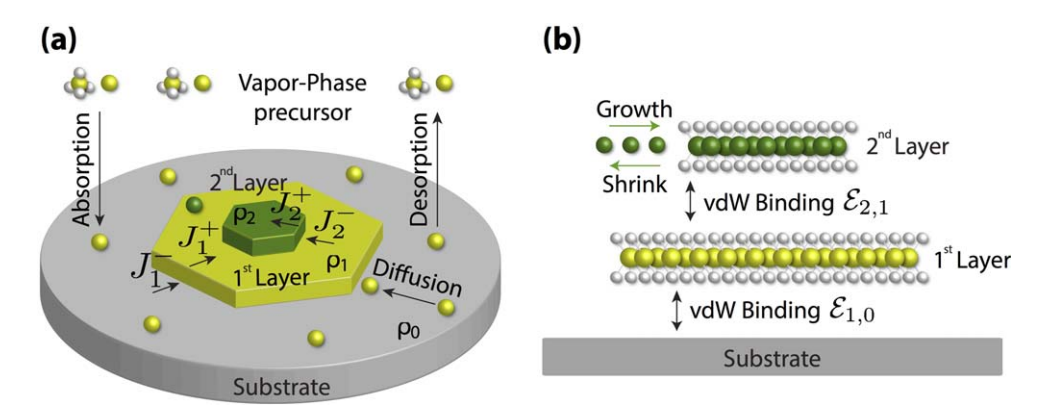


Figure E1. (a) Schematic of epitaxial growth of 2D materials; (b) schematic of vdW interactions between the layers and the substrate.

$$E = \sum_{i=1}^{2} \left(-\int_{\Omega_{i}} \mathcal{E}_{i} dA + \int_{\Gamma_{i}} \gamma_{i} dS \right) + k_{B} T \rho_{ref} \sum_{i=0}^{2} \int_{\Omega_{i}} \frac{\rho_{i}}{\rho_{ref}} \ln \frac{\rho_{i}}{\rho_{ref}} + \left(1 - \frac{\rho_{i}}{\rho_{ref}} \right) \ln \left(1 - \frac{\rho_{i}}{\rho_{ref}} \right) dA,$$
 (1)

where \mathcal{E}_i is the binding energy of layer i that accounts for in-plane bonding and any corresponding vdW interactions. In addition, $\gamma_i = \gamma_i(\theta_i)$ is the edge energy of layer i, θ_i is the normal angle of layer i (e.g. the angle between the normal vector \mathbf{n}_{Γ_i} , which points into Ω_{i-1} , and the x-axis). The function ρ_i is the adatom concentration on layer i and $\rho_{\text{ref}} = \Omega_s$ is the concentration of atomic sites (assumed to be the same on the layers). Further, k_{B} is Boltzmann's constant, T is the temperature and the third term in equation (1) represents the regular solution model free energy.

2.1. Model equations

By requiring mass to be conserved and that the free energy is non-increasing in time, we can derive a thermodynamically-consistent BCF-like system of equations that govern the dynamics of the adatom densities and the layer morphologies and sizes. Here, we only present the nondimensional equations that include several simplifications. A detailed derivation of the equations, a description and justification of the simplifications and the nondimensionalization are given in appendix A.

The nondimensional adatom concentrations satisfy the diffusion equations

$$\partial_t \rho_i = D_i \Delta \rho_i + F_i - \tau_{d,i}^{-1} \rho_i \quad \text{in } \Omega_i, \quad i = 0, 1, 2, \tag{2}$$

where $D_i > 0$ is a dimensionless diffusion coefficient, F_i is a dimensionless deposition flux and $\tau_{d,i}^{-1}$ a dimensionless desorption rate. These are all assumed to be constant. At the layer boundaries Γ_2 and Γ_1 mass conservation is imposed, which yields the kinetic boundary conditions:

$$q_2^+ = -D_2 \nabla \rho_2 \cdot \mathbf{n}_{\Gamma_2} - \rho_2 |_{\Gamma_2} v_2 = k_2^+ (\rho_2 - \rho^* (-\mathcal{E}_2 + \mathcal{E}_1 + \tilde{\gamma}_2 \kappa_2), \tag{3}$$

$$q_2^- = D_1 \nabla \rho_1 \cdot \mathbf{n}_{\Gamma_2} + \rho_1 |_{\Gamma_2} v_2 = k_2^- (\rho_1 - \rho^* (-\mathcal{E}_2 + \mathcal{E}_1 + \tilde{\gamma}_2 \kappa_2), \tag{4}$$

$$q_1^+ := -D_1 \nabla \rho_1 \cdot \mathbf{n}_{\Gamma_1} - \rho_1 |_{\Gamma_1} v_1 = k_1^+ (\rho_1 - \rho^* (-\mathcal{E}_1 + \tilde{\gamma}_1 \kappa_1), \tag{5}$$

$$q_1^- := D_0 \nabla \rho_0 \cdot \mathbf{n}_{\Gamma_1} + \rho_0 |_{\Gamma_1} v_1 = k_1^- (\rho_0 - \rho^* (-\mathcal{E}_1 + \tilde{\gamma}_1 \kappa_1)). \tag{6}$$

Here, q_i^{\pm} are the diffusion fluxes of adatoms to the layer boundaries, with the '+' and '-' subscripts denoting limits from the ith and i-1 layers, ρ^* is a nondimensional measure of the thermodynamic equilibrium density, $\tilde{\gamma}_i = \gamma_i(\theta_i) + \gamma_i''(\theta_i)$, where the primes denote derivatives with respect to θ_i , denotes the layer boundary (edge) stiffness, and κ_i is the curvature of the edge Γ_i (i=1,2). The constants k_i^{\pm} are the dimensionless rates for attachment of adatoms to the edges from the ith (k_i^{+}) and i-1 (k_i^{-}) layers, respectively. The normal velocity of each layer boundary Γ_i is given by

$$v_i = q_i^+ + q_i^- + \beta \partial_s^2 \kappa_i, \tag{7}$$

where the dimensionless constant β is related to the mobility of an adatom along a curved edge. At the boundary of the substrate, we assume there is no flux of adatoms: $\nabla \rho_0 \cdot \mathbf{n}_{\Gamma_0} = 0$.

2.2. Analysis of vdW-BCF model: radial solutions and growth criteria

For simplicity, we consider a configuration in which the two layers and substrate are circular and centered at the same point O. We assume that the edge energy and the kinetic coefficients are isotropic. We solve the system (2)–(7) analytically to derive necessary and sufficient conditions for the growth of layer 2. The layers Ω_1 and Ω_2 have radii $R_1(t)$ and $R_2(t)$. The substrate has radius R_{∞} , which is fixed. We assume that initially $0 < R_2(0) < R_1(0) < R_0$ and that the dynamics are dominated by diffusion so that the time derivative on the left hand side of equation (2) is set to zero (quasi-steady case). We further assume the desorption of adatoms is small and so we set $\tau_{d,i}^{-1} = 0$. The reduced system can be solved analytically. Here, we present only the results, a complete derivation of the solutions is provided in appendix B.

The analytical solutions for the densities ρ_i are:

$$\rho_{2} = -\frac{F_{2}}{4D_{2}}r^{2} + A_{2}\ln(r) + B_{2}, \quad 0 < r < R_{2},$$

$$\rho_{1} = -\frac{F_{1}}{4D_{1}}r^{2} + A_{1}\ln(r) + B_{1}, \quad R_{2} < r < R_{1},$$

$$\rho_{0} = -\frac{F_{0}}{4D_{0}}r^{2} + A_{0}\ln(r) + B_{0}, \quad R_{1} < r < R_{\infty},$$
(8)

where A_i and B_i are given in appendix B. When the flux of adatoms is only non-zero on the substrate (e.g. $F_0 \ge 0$, $F_2 = F_1 = 0$), which reflects the catalytic decomposition of CH₄ vapor on the substrate surface into mobile radicals (e.g. CH and C) that can attach to the graphene layers [24], the normal velocities of the layer boundaries are given by

$$v_1 = \frac{\mathrm{d}}{\mathrm{d}t} R_1(t) = \frac{F_0}{2R_1} (R_\infty^2 - R_1^2) - \frac{R_2}{R_1} v_2, \tag{9}$$

$$v_2 = \frac{\mathrm{d}}{\mathrm{d}t} R_2(t) = \frac{D_1 \rho^* \left(-\mathcal{E}_2 + 2\mathcal{E}_1 + \frac{\gamma_2}{R_2} - \frac{\gamma_1}{R_1} \right)}{R_2 \left(\ln \frac{R_2}{R_1} - \frac{D_1}{k_2 R_2} - \frac{D_1}{k_1^+ R_1} \right)},$$
(10)

where γ_1 and γ_2 are isotropic edge energies. The velocities for the more general case with F_1 and F_2 not necessarily equal to zero can be found in appendix B. Define $\mathcal{E}_{2,1} = \mathcal{E}_2 - \mathcal{E}_1$ to be the binding energy density between the two layers and $\mathcal{E}_{1,0} = \mathcal{E}_1$ to be the binding energy

density between layer 1 and the substrate. The difference between these two energies

$$\Delta \mathcal{E} = \mathcal{E}_{2,1} - \mathcal{E}_{1,0} = \mathcal{E}_2 - 2\mathcal{E}_1,\tag{11}$$

is the gain in energy by adding atoms to layer 2 instead of layer 1. An analysis of v_2 in equation (10) reveals a sufficient condition for the growth of layer 2:

$$\Delta \mathcal{E} > \frac{\gamma_2}{R_2} - \frac{\gamma_1}{R_1},\tag{12}$$

since the denominator in equation (10) is always non-positive. This is analogous to the growth criterion derived in [14] for faceted layers. This condition states that the difference between the binding energies, $\Delta \mathcal{E}$, must be large enough to overcome the energy penalty of increasing the layer perimeter. It follows that if $R_2 > R_{2,c} := \gamma_2/\Delta \mathcal{E}$, then layer 2 always grows, regardless of the size of layer 1. This is analogous to a critical nucleation size. Further, if $R_1 > R_{1,c} := \frac{\gamma_1}{\gamma_2/R_2 - \Delta \mathcal{E}}$ then layer 2 always shrinks. When R_2 is close to $R_{2,c}$, layer 2 may grow due to kinetic effects. That is, R_2 may surpass $R_{2,c}$ before R_1 surpasses $R_{1,c}$. Whether this occurs depends on the values of the parameters. For example, slowing down the growth of the first layer (e.g. by decreasing F_0) or increasing the rate of growth of the second layer (e.g. by increasing D_1 , k_2^- or k_1^+) increases the region of kinetically-driven growth. We call $R_{2,k}$ the kinetic critical radius—that is, if $R_{2,c} > R_2(0) > R_{2,k}$, then the second layer grows due to the kinetics of the system.

By solving for the radii R_1 and R_2 numerically and varying the initial radii, we can estimate $R_{2,k}$ numerically and construct a phase diagram for the growth of the 2nd layer. As an example, we fix the parameters $\Delta \mathcal{E} = 0.05$, $F_0 = 0.1$, $\gamma_1 = \gamma_2 = 0.01$, $\rho^* = 0.5$, $D_1 = 1$, $k_2^- = k_1^+ = 0.5$ and $R_{\infty} = 3.8$. We then vary the initial sizes of the layers $R_1(0)$ and $R_2(0)$, keeping $R_2(0) \geqslant R_1(0)$. The resulting phase diagram is shown in figure E2(a). Also observe that for R_2 in between $R_{1,c}$ and $R_{2,k}$, the 2nd layer grows transiently before shrinking to zero size. Example trajectories of the layer dynamics are shown in figure E2(b).

3. Reformulation of the vdW-BCF model of multilayer growth using the diffuse domain method

To solve the vdW-BCF equations for unconstrained layer geometries, we reformulate the system using the diffuse domain method (DDM). Here, we combine and extend the approaches from [21, 23] to develop a fully-second order accurate DDM for the vdW-BCF system. We embed the substrate and layer domains into a larger, rectangular domain $\tilde{\Omega}$ and we introduce a diffuse domain function φ to mark the locations of the layers and substrate (e.g. approximate atomic height). In particular, $\varphi \approx 0$ in the substrate (Ω_0), $\varphi \approx 1$ in layer 1 (Ω_1) and $\varphi \approx 2$ in layer 2 (Ω_2).

In order to facilitate comparisons with theory from the previous section, we assume that the outer boundary of the substrate is circular and so we introduce another diffuse domain function φ_{∞} to identify the deposition domain $\Omega = \Omega_0 \cup \Omega_1 \cup \Omega_2$, where $\varphi_{\infty} \approx 1$, within the larger domain $\tilde{\Omega}$. See figure E3(a). The diffuse domain variables change rapidly but smoothly across the boundaries (e.g. steps) as shown in figure E3(b). The width of these narrow transition layers is $\approx \epsilon$, a small parameter. The boundaries of the substrate and layers 1 and 2 correspond to $\varphi \approx 0.5$ and $\varphi \approx 1.5$, respectively. The kinetic boundary conditions are incorporated via source terms and the dynamics of the layers are captured by evolving the diffuse domain function φ . In addition, we follow [23] and solve only two adatom diffusion equations in the extended domain $\tilde{\Omega}$. A brief description of the derivation and an asymptotic

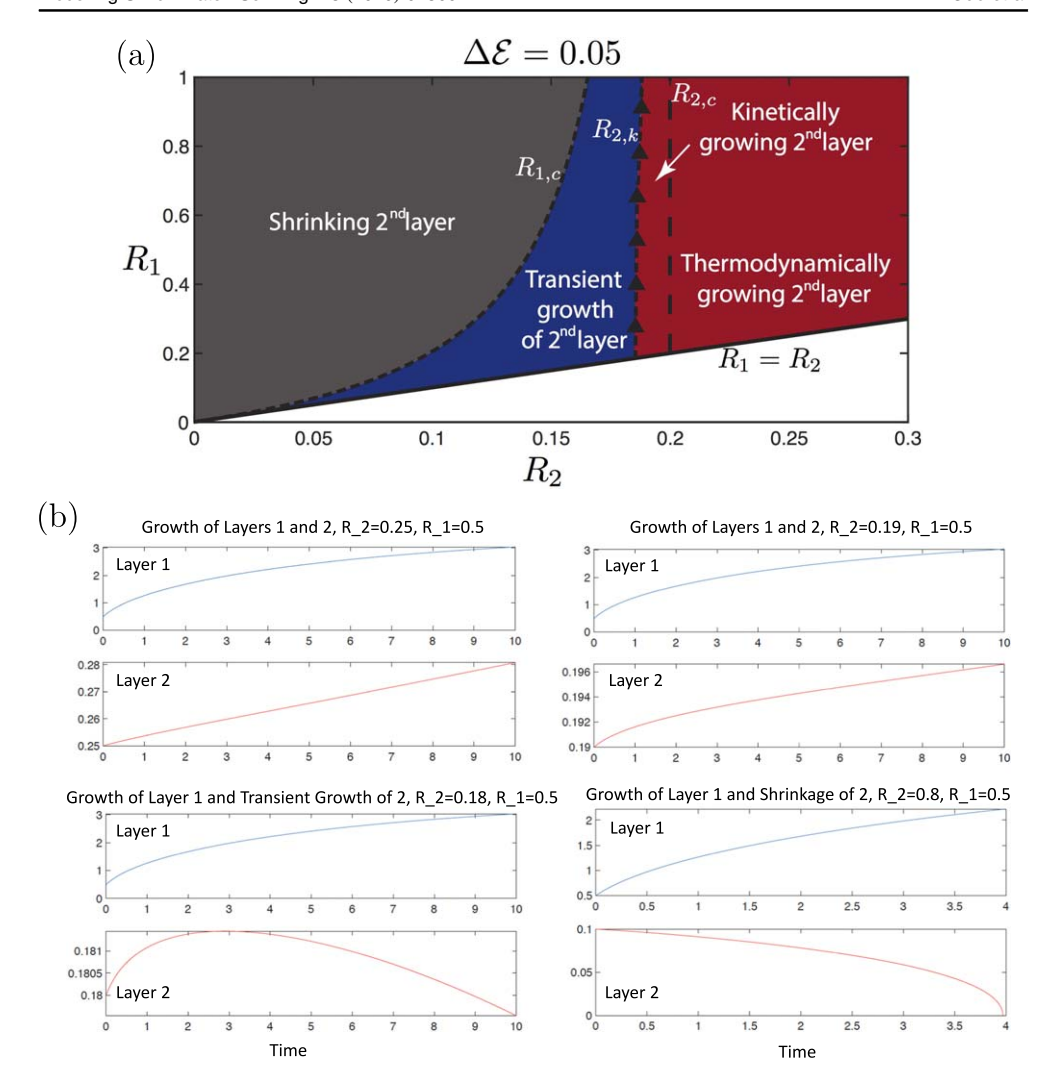


Figure E2. (a) Morphology diagram, assuming that the layers are circular, showing the dependence of layer 2 growth on the size of layers 1 and 2. In particular, the sign of v_2 is shown for different sizes of the layers (R_1, R_2) . When $R_2 > R_{2,c}$ layer 2 always grows. When $R_1 > R_{1,c}$ layer 2 always shrinks. When $R_{1,c} < R_2 < R_{2,k}$ layer 2 grows transiently before shrinking. When $R_2 > R_{2,k}$ layer 2 grows because R_2 increases past $R_{2,c}$ sooner than R_1 crosses $R_{1,c}$. See text for details on $R_{1,c}$, $R_{2,k}$ and $R_{2,c}$. (b) Sample trajectories of the layer radii R_1 and R_2 in time, starting from different initial radii. The parameters are as in equation (42) except with $\mathcal{E}_2 = 1.05$ so that $\Delta \mathcal{E} = 0.05$.

analysis of the vdW-BCF-DDM, which demonstrates that the vdW-BCF-DDM system approximates the sharp interface vdW-BCF model to $O(\epsilon^2)$, are given in appendix C. Here, we present only the resulting equations:

$$(\varphi_{\infty} H_0(\varphi) \rho_0^{\epsilon})_t = \nabla \cdot (\varphi_{\infty} H_0(\varphi) D_0(\varphi) \nabla \rho_0^{\epsilon}) + \varphi_{\infty} H_0(\varphi) F_0(\varphi) - \varphi_{\infty} H_0(\varphi) \tau_d^{-1} \rho_0^{\epsilon} - \varphi_{\infty} |\nabla \varphi| k_0(\varphi) (\rho_0^{\epsilon} - \rho^* (\mathcal{E}(\varphi) + \epsilon^{-1} \gamma(\varphi) \mu),$$
(13)

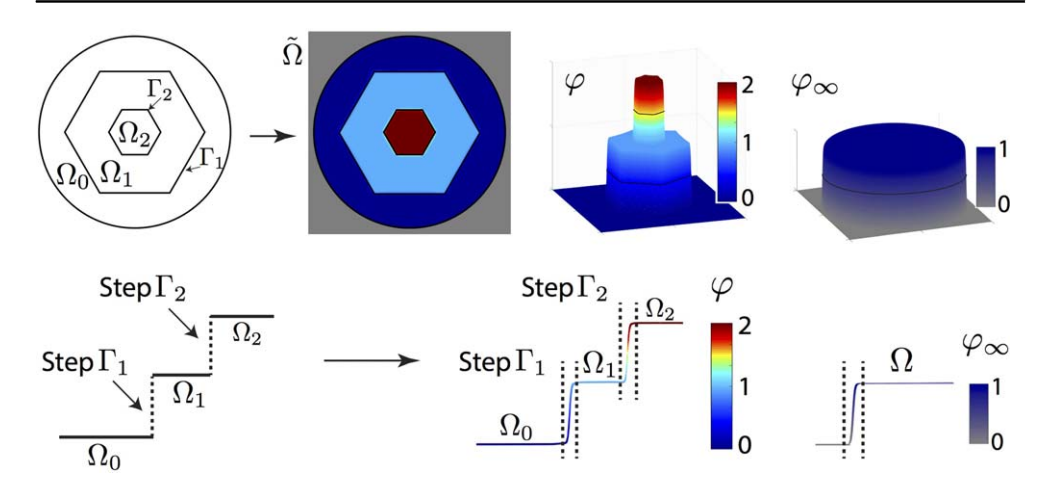


Figure E3. Schematic of the diffuse domain method. Top: the sharp (physical) interface domain is embedded in a larger, square domain $\tilde{\Omega}$ where a phase-field functions ϕ and ϕ_{∞} approximate the height of the layers and the characteristic function of the deposition domain, respectively. Bottom: a slice across the sharp interface domain and slices of the phase-field functions φ and φ_{∞} .

$$(\varphi_{\infty} H_{1}(\varphi) \rho_{1}^{\epsilon})_{t} = \nabla \cdot (\varphi_{\infty} H_{1}(\varphi) D_{1} \nabla \rho_{1}^{\epsilon}) + \varphi_{\infty} H_{1}(\varphi) F_{1}$$
$$- \varphi_{\infty} H_{1}(\varphi) \tau_{d}^{-1} \rho_{1}^{\epsilon} - \varphi_{\infty} |\nabla \varphi| k_{1}(\varphi) (\rho_{1}^{\epsilon} - \rho^{*} (\mathcal{E}(\varphi) + \epsilon^{-1} \gamma(\varphi) \mu), \tag{14}$$

where the kinetic boundary conditions (3)–(6) are modeled by the extra source terms containing $|\nabla \varphi|$, which approximates the surface delta function. Equation (13) models the adatom diffusion equations on the substrate and layer 2, e.g. ρ_0^ϵ approximates the adatom concentration on both the substrate, where $\varphi \approx 0$, and layer 2, where $\varphi \approx 2$. Equation (14) models adatom diffusion on layer 1 and ρ_1^ϵ is the corresponding approximate adatom concentration. For simplicity, we have assumed $\tau_{d,i} = \tau_d$. The functions H_0 , H_1 are extended approximate characteristic functions of the layer domains and substrate. In particular, H_0 is the approximate characteristic function of the substrate and layer 2:

$$H_0(\varphi) = \begin{cases} 1 - \varphi & \text{for } \varphi \in [0, 1], \\ \varphi - 1 & \text{for } \varphi \in (1, 2], \end{cases}$$
 (15)

and H_1 is the approximate characteristic function of layer 1:

$$H_{1}(\varphi) = \begin{cases} \varphi & \text{for } \varphi \in [0, 1], \\ 2 - \varphi & \text{for } \varphi \in (1, 2]. \end{cases}$$
 (16)

Further, the flux $F_0(\varphi)$ corresponds to the flux on the substrate

$$F_0(\varphi) = \begin{cases} F_0 & \text{for } \varphi < \epsilon, \\ 0 & \text{for } \varphi \in [\epsilon, 2], \end{cases}$$
 (17)

and $D_0(\varphi)$ corresponds to the adatom diffusion coefficients on the substrate and layer 2

$$D_0(\varphi) = \begin{cases} D_0 & \text{for } \varphi \in [0, 1], \\ D_2 & \text{for } \varphi \in (1, 2]. \end{cases}$$
 (18)

Analogously, the extended vdW energies and kinetic attachment rates are defined as

$$\mathcal{E}(\varphi) = \begin{cases} -\mathcal{E}_1 & \text{for } \varphi \in [0, 1], \\ -\mathcal{E}_2 + \mathcal{E}_1 & \text{for } \varphi \in (1, 2], \end{cases}$$
 (19)

and

$$k_0(\varphi) = \begin{cases} k_1^- & \text{for } \varphi \in [0, 1], \\ k_2^+ & \text{for } \varphi \in (1, 2], \end{cases}$$
 (20)

$$k_{\mathbf{l}}(\varphi) = \begin{cases} k_{\mathbf{l}}^{+} & \text{for } \varphi \in [0, 1], \\ k_{\mathbf{l}}^{-} & \text{for } \varphi \in (1, 2]. \end{cases}$$
 (21)

The evolution of the layers is implicitly captured by evolving φ :

$$\partial_{t}\varphi = |\nabla\varphi|(k_{0}(\varphi)(\rho_{0}^{\epsilon} - \rho^{*}(\mathcal{E}(\varphi) + \epsilon^{-1}\gamma(\varphi)\mu) + k_{1}(\varphi)(\rho_{1}^{\epsilon} - \rho^{*}(\mathcal{E}(\varphi) + \epsilon^{-1}\gamma(\varphi)\mu)) + \epsilon^{-2}\beta\nabla\cdot(G(\varphi)\nabla\mu),$$
(22)

$$\mu = -\epsilon^2 \Delta \varphi + B'(\varphi), \tag{23}$$

where the right hand side of equation (22) models the normal velocity from equation (7). Note that since the outer boundary of the substrate does not change we do not need to pose an evolution equation for φ_0 . In equations (22) and (23), $G(\varphi) = 2B(\varphi)$ is an extended double well potential:

$$B(\varphi) = \begin{cases} 18\varphi^2(\varphi - 1)^2 & \text{for } \varphi \in [0, 1], \\ 18(\varphi - 1)^2(\varphi - 2)^2 & \text{for } \varphi \in (1, 2]. \end{cases}$$
 (24)

As shown in appendix C, and confirmed by our numerical results in the next section, the vdW-BCF-DDM system is second order accurate with respect to the interface thickness ϵ . Moreover, our diffuse interface model can be extended to simulate the more nonlinear model derived in appendix A and to simulate an arbitrary number of vertically-stacked layers (see appendix A.5).

Finally, at the boundary of the larger domain $\partial \tilde{\Omega}$, we take the conditions

$$\nabla \rho_0^{\epsilon} \cdot \mathbf{n} = \nabla \rho_1^{\epsilon} \cdot \mathbf{n} = \nabla \varphi \cdot \mathbf{n} = \nabla \mu \cdot \mathbf{n} = 0. \tag{25}$$

The model is insensitive, however, to the choice of boundary conditions on $\partial \tilde{\Omega}$.

4. Numerical results

To solve the vdW-BCF-DDM system (13)–(25) numerically, we develop a mass-conservative, semi-implicit, second-order accurate, adaptive finite-difference method using Crank-Nicholson discretization in time and centered differences in space, by extending our previous work, e.g. [25]. To solve the nonlinear discrete system at the implicit time level, we use a full approximation storage (FAS) nonlinear multigrid method. Block-structured adaptive mesh refinement is utilized to efficiently discretize the system. The details of the method are provided in appendix D.

We begin by considering the isotropic, quasi-steady case so we may compare our numerical results to the analytical solutions presented in section 2.2 to validate the accuracy of our approximations. We then consider time-dependent diffusion and anisotropic edge

energies and kinetic coefficients. We perform parametric studies to determine the effect of parameters on the growth and morphologies of the layers.

4.1. Quasi-stationary dynamics

We consider the same set up as in section 2.2. Initially, two layers are centered at the origin with different radii R_1 and R_2 and the edge energy and kinetic coefficients are isotropic. The two islands are bounded by a larger circular substrate with radius R_0 . The initial condition for the diffuse domain variable is

$$\varphi(x, 0) = \frac{1}{2} \left(1 - \tanh\left(\frac{3(x - R_1)}{\epsilon}\right) \right) + \frac{1}{2} \left(1 - \tanh\left(\frac{3(x - R_2)}{\epsilon}\right) \right), \quad (26)$$

such that $\varphi \approx 1$ approximates layer 1 and $\varphi \approx 2$ approximates layer 2. We take

$$\varphi_{\infty}(x) = \frac{1}{2} \left(1 - \tanh\left(\frac{3(x - R_0)}{\epsilon}\right) \right),\tag{27}$$

which corresponds to the region containing the substrate and the two layers where deposition and growth take place. The parameter ϵ is the thickness of the layer and substrate boundaries. The initial radii of the layers are $R_1(0) = 1.2$ and $R_2(0) = 0.6$. The outer radius of the substrate is $R_{\infty} = 1.8$. The physical parameters are taken to be

$$k_1^{\pm} = k_2^{\pm} = 1, \quad \rho^* = 0.01, \quad \gamma_1 = \gamma_2 = 1, \quad D_0 = D_1 = D_2 = 1, \quad F_0 = F_1 = F_2 = 2,$$

 $\tau_d^{-1} = 0, \quad \beta = 0, \quad \mathcal{E}_1 = -1, \quad \mathcal{E}_2 = -2.$ (28)

The computations are carried out on a square domain $[-2, 2] \times [-2, 2]$. A four-level adaptive mesh is employed, which consists of a root level with mesh size h_0 and three refinement levels above it so that the finest mesh size $h_3 = h_0/8$. In order to test the convergence rate corresponding to different values of ϵ , we refine the root level grid size h_0 and ϵ together, and hence all the finer level grid sizes h_1 , h_2 and h_3 are refined as well. In particular, we set $h_3 = \frac{\epsilon}{6.4}$. The mesh is refined according to values of $|\nabla \varphi| + |\nabla \varphi_0|$ over the entire domain (see appendix D). The time step is taken to be $\Delta t = \frac{\epsilon}{0.8} \times 10^{-4}$ to ensure that the time errors are small compared to spatial errors; the method is stable (and accurate) for larger time steps.

Five different values of ϵ are used for the convergence test, namely, $\epsilon_1 = 0.8$, $\epsilon_2 = 0.4$, $\epsilon_3 = 0.2$, $\epsilon_4 = 0.1$ and $\epsilon_5 = 0.05$. The difference between the analytical solutions and our numerical results are computed using the following metrics:

$$E_{\epsilon,\rho_k}^{(2)} = \frac{||\varphi(\rho_k^{\epsilon} - \rho_k)||_{\ell_2}}{||\varphi\rho_k||_{\ell_2}} \text{ and } E_{\epsilon,\rho_k}^{(\infty)} = \frac{||\varphi(\rho_k^{\epsilon} - \rho_k)||_{\ell_\infty}}{||\varphi\rho_k||_{\ell_\infty}},$$
(29)

where k=0 denotes the substrate and k=1, 2 denote the layers. The convergence rate is obtained by $r_{i-1}=\ln E^{(\cdot)}_{\epsilon_i,\rho_k}/E^{(\cdot)}_{\epsilon_{i-1},\rho_k}$, where ϵ_i and ϵ_{i-1} represent consecutive values of ϵ . The horizontal slices of the adatom concentrations ρ_k^ϵ for different ϵ together with the analytical solution are shown at time t=0.1 in figure E4(a). We can observe that the numerical results approach the analytical solution as ϵ decreases. The corresponding errors and rates of convergence are presented in table 1, which indicates that the numerical method converges to the analytic solution with an overall second order convergence rate in both the ℓ_2 and ℓ_∞ norms, as predicted by the asymptotic analysis in appendix $\mathbb C$.

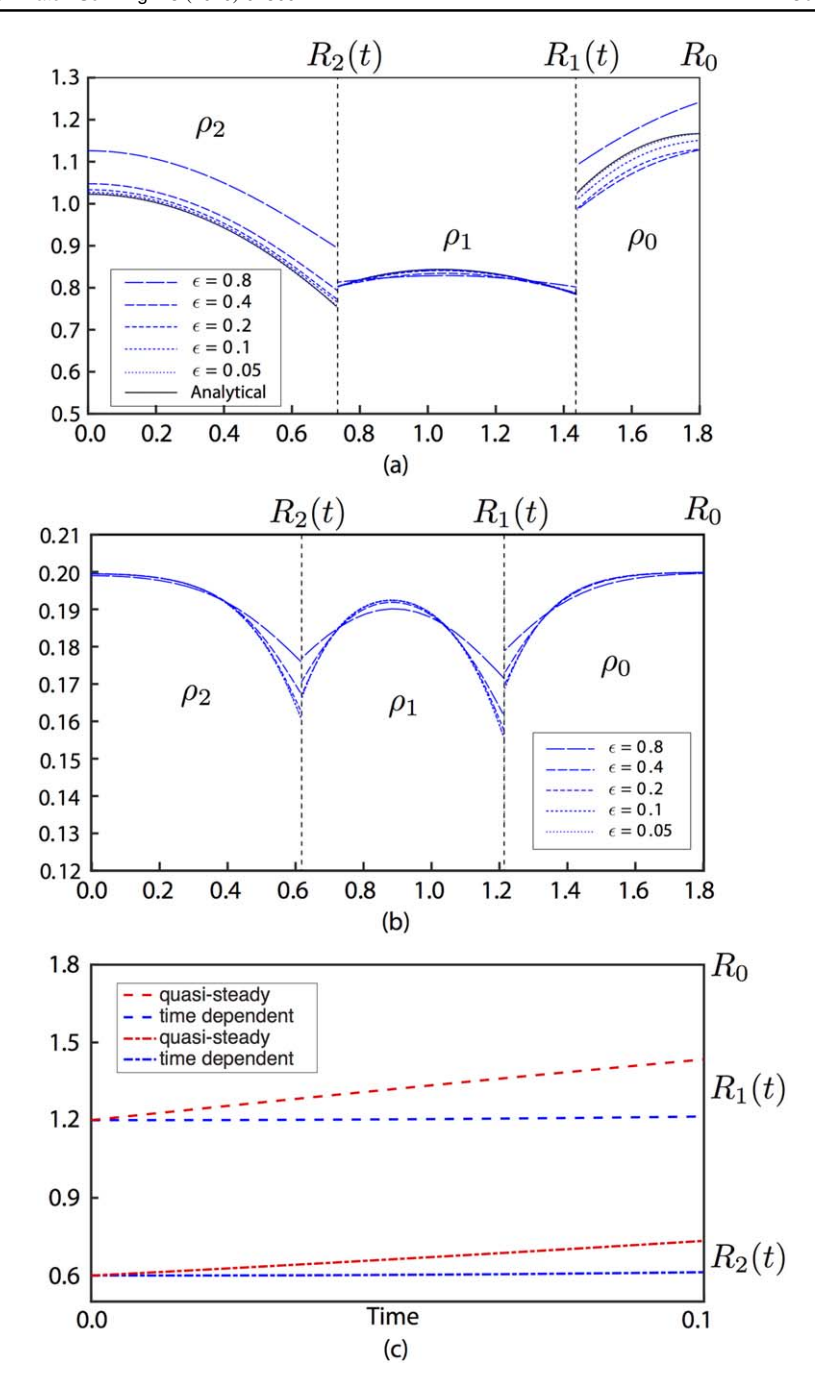


Figure E4. Comparisons between the numerical results and analytical solution at time t=0.1. In (a) the quasi-steady dynamics are shown from section 4.1. In (b) the fully-time dependent dynamics are shown from section 4.2. The dashed and dotted lines represent the horizontal slices of densities ρ_2 , ρ_1 and ρ_0 at different ϵ , as labeled. In (a) the black solid lines give the analytical solution. The radii of the layers are shown as a function of time in (c) the adatom concentrations and gradients are larger in the quasi-steady case, which give rise to faster dynamics in the quasi-steady case.

t = 0.10 $E_{\epsilon,\rho}^{(2)}$ $E_{\epsilon,\rho_0}^{(2)}$ Rate Rate Rate 0.8 5.252×10^{-2} 5.143×10^{-2} 2.095×10^{-1} $1.514\,\times\,10^{-2}$ 2.020×10^{-2} 6.557×10^{-2} 1.80 0.4 1.35 1.66 3.229×10^{-3} 3.858×10^{-3} 1.529×10^{-2} 0.2 2.23 2.40 2.10 8.198×10^{-4} 9.945×10^{-4} 4.198×10^{-3} 0.1 1.98 1.96 1.87 0.05 1.801×10^{-4} 2.12 2.411×10^{-4} 2.04 1.001×10^{-3} 2.07 t = 0.10 ℓ_{∞} $E_{\epsilon,\rho_2}^{(\infty)}$ $E_{\epsilon,\rho_1}^{(\infty)}$ $E_{\epsilon,\rho_0}^{(\infty)}$ Rate ϵ Rate Rate 0.8 6.132×10^{-2} 5.812×10^{-1} $3.271 \times 10^{-}$ 1.914×10^{-2} 2.360×10^{-2} 1.214×10^{-1} 0.4 1.68 1.30 1.43 5.058×10^{-3} 3.368×10^{-2} 0.2 1.92 5.429×10^{-3} 2.12 1.85 1.453×10^{-3} 1.496×10^{-3} 1.058×10^{-2} 0.1 1.80 1.67 1.86 3.946×10^{-4} 4.007×10^{-4} 2.996×10^{-3} 0.05 1.88 1.90 1.82

Table 1. Convergence test for the adatom concentrations ρ_2 , ρ_1 and ρ_0 under quasisteady dynamics from section 4.1.

4.2. Fully time-dependent case

Next, we include the time derivatives in the adatom diffusion equations. The physical parameters, the computational domain and the numerical parameters are the same as in the previous section. Since we do not have an analytic solution in this case, we compare the results obtained using different ϵ (and hence h_0) with each other. The horizontal slices of the adatom concentrations ρ_2^{ϵ} , ρ_1^{ϵ} and ρ_0^{ϵ} are shown at time t=0.1 in figure E4(b). Compared to the quasi-steady case, the adatom concentrations in each layer are smaller and there is less variation across the layers. Correspondingly, the layers do not move as rapidly in the time-dependent case with the first layer growing more slowly than the second, compared to the quasi-steady case (figure E4(c)). Figure E4(b) also shows that the results converge as ϵ is decreased. To estimate the accuracy and quantify the rate of convergence, we define the consecutive errors as

$$\begin{split} E_{\epsilon_{i-1},\epsilon_{i},\rho_{2}}^{(2)} &= ||\varphi_{2}(\rho_{2}^{\epsilon_{i-1}} - \rho_{2}^{\epsilon_{i}})||_{\ell_{2}}, \qquad E_{\epsilon_{i-1},\epsilon_{i},\rho_{2}}^{(\infty)} &= ||\varphi_{2}(\rho_{2}^{\epsilon_{i-1}} - \rho_{2}^{\epsilon_{i}})||_{\ell_{\infty}} \\ E_{\epsilon_{i-1},\epsilon_{i},\rho_{1}}^{(2)} &= ||\varphi_{1}(\rho_{1}^{\epsilon_{i-1}} - \rho_{1}^{\epsilon_{i}})||_{\ell_{2}}, \qquad E_{\epsilon_{i-1},\epsilon_{i},\rho_{1}}^{(\infty)} &= ||\varphi_{1}(\rho_{1}^{\epsilon_{i-1}} - \rho_{1}^{\epsilon_{i}})||_{\ell_{\infty}}, \\ E_{\epsilon_{i-1},\epsilon_{i},\rho_{0}}^{(2)} &= ||\varphi_{\infty}(\rho_{0}^{\epsilon_{i-1}} - \rho_{0}^{\epsilon_{i}})||_{\ell_{2}}, \qquad E_{\epsilon_{i-1},\epsilon_{i},\rho_{0}}^{(\infty)} &= ||\varphi_{\infty}(\rho_{0}^{\epsilon_{i-1}} - \rho_{0}^{\epsilon_{i}})||_{\ell_{\infty}}, \end{split}$$
(30)

where the φ_j , with j=0, 1 and 2 are the approximate characteristic functions on the substrate, layer 1 and layer 2 respectively. They are defined as

$$\varphi_2 = \begin{cases} \varphi - 1 & \text{for } \varphi \in (1, 2], \\ 0 & \text{for } \varphi \in [0, 1], \end{cases}$$
(31)

$$\varphi_1 = \sqrt{(1 - \sqrt{(\varphi - 1)^2})^2},$$
(32)

$$\varphi_{\infty} = \begin{cases} 0 & \text{for } \varphi \in (1, 2], \\ \varphi_{\infty}(1 - \varphi) & \text{for } \varphi \in [0, 1], \end{cases}$$
(33)

acpendent	dynamics in sec	11011 4.2	•			
t = 0.10	ℓ_2					
ϵ	$E^{(2)}_{\epsilon_{i-1},\epsilon_i, ho_2}$	Rate	$E^{(2)}_{\epsilon_{i-1},\epsilon_i, ho_1}$	Rate	$E^{(2)}_{\epsilon_{i-1},\epsilon_i, ho_0}$	Rate
0.4	3.978×10^{-3}		8.066×10^{-3}		5.648×10^{-3}	
0.2	2.315×10^{-3}	0.78	3.299×10^{-3}	1.29	2.224×10^{-3}	1.35
0.1	6.977×10^{-4}	1.73	9.287×10^{-4}	1.83	5.779×10^{-4}	1.94
0.05	1.781×10^{-4}	1.97	2.258×10^{-4}	2.04	1.239×10^{-4}	2.22
t = 0.10	ℓ_{∞}					
ϵ	$E_{\epsilon_{i-1},\epsilon_i, ho_2}^{(\infty)}$	Rate	$E_{\epsilon_{i-1},\epsilon_{i}, ho_{1}}^{(\infty)}$	Rate	$E^{(\infty)}_{\epsilon_{i-1},\epsilon_i, ho_0}$	Rate
0.4	4.316×10^{-3}		4.167×10^{-3}	_	3.241×10^{-3}	
0.2	2.521×10^{-3}	0.78	2.299×10^{-3}	0.86	1.816×10^{-3}	0.84
0.1	9.029×10^{-4}	1.48	8.187×10^{-4}	1.49	6.444×10^{-4}	1.49
0.05	2.606×10^{-4}	1.80	2.368×10^{-4}	1.80	1.892×10^{-4}	1.77

Table 2. Convergence test for concentrations ρ_2 , ρ_1 and ρ_0 under the fully time-dependent dynamics in section 4.2.

and these functions are evaluated at $\epsilon = \epsilon_i$. The errors and rates of convergence, which are calculated from the consecutive errors at time t=0.1 in an analogous way as in the previous section, are presented in table 2. As in the quasi-steady case, we observe that the results converge with second order accuracy in both the ℓ_2 and ℓ_∞ norms.

4.3. Anisotropic dynamics

We now consider the case in which the edge energies and kinetic coefficients are anisotropic:

$$k_0(\varphi, \theta) = \begin{cases} k_2^+ \xi_k(\theta) & \text{for } \varphi \in (1, 2], \\ k_1^- \xi_k(\theta) & \text{for } \varphi \in [0, 1], \end{cases}$$
(34)

$$k_{1}(\varphi, \theta) = \begin{cases} k_{2}^{-} \xi_{k}(\theta) & \text{for } \varphi \in (1, 2], \\ k_{1}^{+} \xi_{k}(\theta) & \text{for } \varphi \in [0, 1], \end{cases}$$

$$(35)$$

where

$$\xi_k(\theta) = 1 - \epsilon_{k,n} \cos(n(\theta - \theta_0)), \tag{36}$$

is the kinetic coefficient anisotropy function, θ is the normal angle (e.g. angle between the normal vector and the *x*-axis), and θ_0 is a reference angle which is taken to be $\theta_0 = \pi/n$. The edge energies are defined analogously:

$$\gamma(\theta) = \gamma(\xi_s(\theta) + \xi_s''(\theta)),\tag{37}$$

$$\xi_s(\theta) = 1 - \epsilon_{s,n} \cos(n\theta), \tag{38}$$

where ξ_s is the edge energy anisotropy function. The coefficients $\epsilon_{k,n}$ and $\epsilon_{s,n}$ measure the anisotropy strengths. In this paper, we only consider three-fold (n=3) and six-fold (n=6) anisotropies, which reflect the symmetries of MoS₂ and graphene multilayers, respectively. The trigonometric functions are calculated using φ :

$$\cos(\theta) = \frac{\varphi_x}{\sqrt{\varphi_x^2 + \varphi_y^2 + \delta}}, \quad \text{and} \quad \sin(\theta) = \frac{\varphi_y}{\sqrt{\varphi_x^2 + \varphi_y^2 + \delta}}, \quad (39)$$

where we introduce a small parameter $\delta = 10^{-6}$ to avoid singularities. Then, $\cos(3\theta)$ and $\cos(6\theta)$ can be calculated using the trigonometric identites:

$$\cos(6\theta) = 2\cos^2(3\theta) - 1, \quad \cos(3\theta) = \cos\theta \cdot (2\cos(2\theta) - 1), \tag{40}$$

$$\cos(2\theta) = \cos^2\theta - \sin^2\theta = \frac{\varphi_x^2 - \varphi_y^2}{\varphi_x^2 + \varphi_y^2 + \delta}.$$
 (41)

We next consider the quasi-steady dynamics of two anisotropic layers. Initially, the layers are taken to be circular with radii $R_1(0) = 1.0$ and $R_2(0) = 0.2$. The outer boundary of the substrate is $R_{\infty} = 3.8$. The physical parameters are taken to be:

$$k_1^{\pm} = k_2^{\pm} = 0.5, \quad \rho_1^* = 0.5, \quad \gamma_1 = \gamma_2 = 0.01, \quad D_0 = D_1 = D_2 = 1, \quad F_0 = 0.1,$$

 $F_1 = F_2 = 0, \quad \tau_d^{-1} = 0, \quad \beta = 1.11 \times 10^{-5}, \quad \mathcal{E}_1 = 0.5, \quad \mathcal{E}_2 = 1.4.$ (42)

Note that unlike the previous examples, the only non-zero flux is on the substrate F_0 , which as discussed before reflects the assumption that the reactions to produce the attaching species occur only on the substrate surface [24]. Note that $\Delta \mathcal{E} = 0.4$ and $\gamma_2/R_2(0) - \gamma_1/R_1(0) = 0.04$ so that growth would occur under isotropic, quasi-steady dynamics (recall the growth condition in equation (12)). The parameters for the anisotropy are set as

$$n = 6, \quad \epsilon_{k,n} = 0.3, \quad \epsilon_{s,n} = 0.01,$$

 $n = 3, \quad \epsilon_{k,n} = 0.7, \quad \epsilon_{s,n} = 0.01.$ (43)

The morphologies of the growing layers are shown in figure E5(a). In both the six-fold and three-fold anisotropic cases, layers 1 and 2 grow. In the six-fold case, the layers are nearly faceted at early times while the corners are smoothed slightly from the surface diffusion. At later times, both layers develop negative curvature. In the three-fold case, layer 1 evolves to a convex triangular shape at early times while layer 2 develops negative curvature early on. At later times, the corners of layer 1 somewhat elongate with their curvature being set by the surface diffusion coefficient (see figure E9(c)). The corresponding adatom concentrations are shown in figure E5(b) where we see the adatoms diffusing toward both layers driving their growth. In figure E5(c), the adaptive mesh is shown for the six-fold anisotropic case. Observe that there is a fine mesh near the outer boundary of the substrate, which does not change. The mesh near the boundaries of layers 1 and 2 is dynamically refined and and the mesh in the bulk regions is coarsened. In the anisotropic case, we also observe second-order accurate convergence in ℓ_2 and ℓ_{∞} , see appendix E.

4.4. Parameter studies

We next investigate the effects of the physical parameters on the growth of the layers. In particular, we consider the binding energy differences $\Delta \mathcal{E}$, the edge energy γ and the surface diffusion β , flux F_0 and the kinetic attachment rates k_2^- and k_1^+ . We fix all the other parameters as in equation (42) and describe only those parameters that are changed.

4.4.1. Binding energy differences. We first investigate the effects of $\Delta \mathcal{E}$ on the growth rate of layer 2. The morphologies and adatom concentrations for six-fold anisotropic layers obtained from the quasi-steady dynamics are shown in figures E6(a) and (b), respectively.

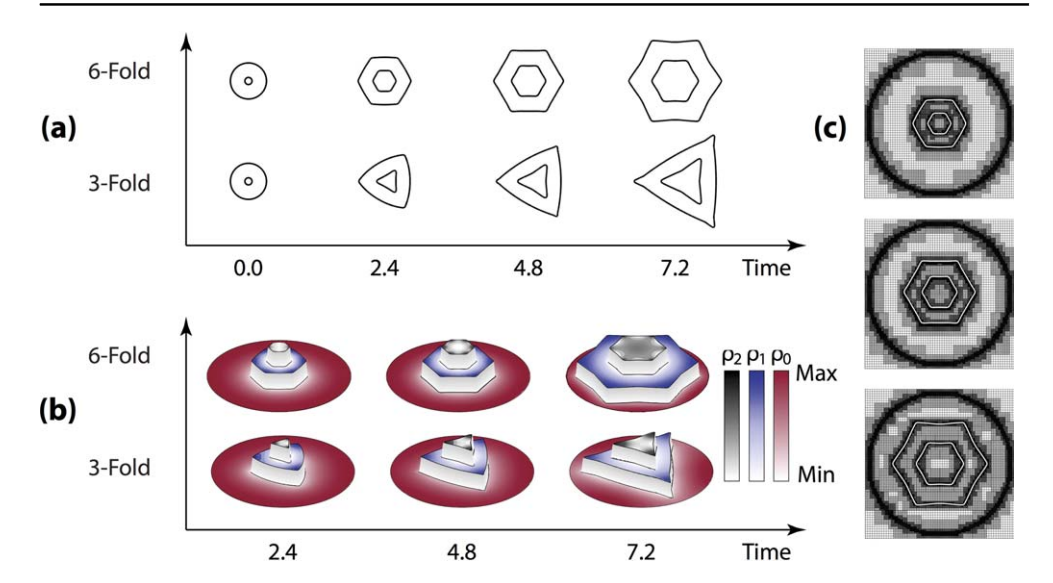


Figure E5. The quasi-steady dynamics of layers 1 and 2 using six-fold and three-fold symmetric anisotropic edge energies and kinetic coefficients under conditions for which both layers should grow. See text for parameters. (a) Time evolution of the layer morphologies; (b) time evolution of the adatom concentrations on the layers. (c) The dynamic adaptive mesh for six-fold anisotropic layers. As both layers grow, driven by fluxes of the adatoms, negative curvatures develop in both layers in the six-fold case and in layer 2 in the three-fold case. The corners of the layers are more affected by surface diffusion in the three-fold case compared to the six-fold case.

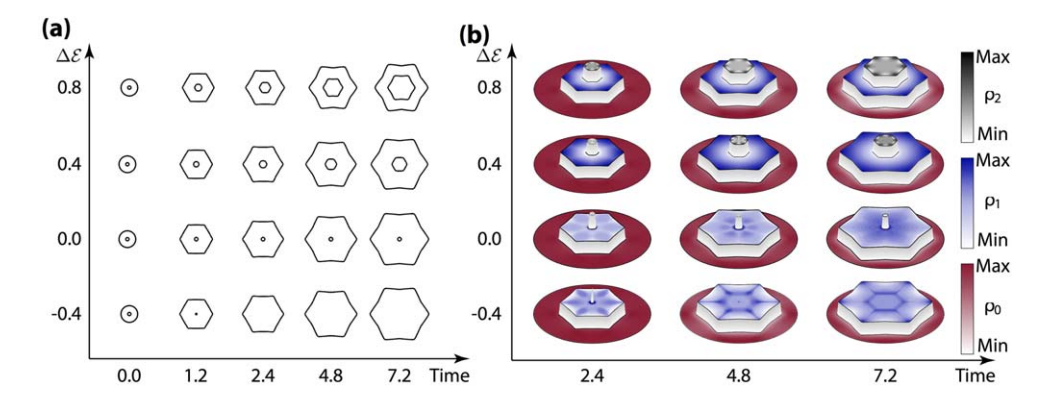


Figure E6. The effects of binding energy differences $\Delta \mathcal{E}$ for the quasi-steady dynamics of layers 1 and 2 using six-fold symmetric anisotropic edge energies and kinetic coefficients. See text for other parameters. (a) Time evolution of the layer morphologies; (b) Time evolution of the adatom concentrations on the layers. The growth conditions for six-fold anisotropic layers follow the thermodynamic criterion in equation (12), derived in the isotropic, quasi-steady case (circular layers), that relates $\Delta \mathcal{E}$ and the sizes of the layers. Further, when layer 2 grows, it does so at the expense of layer 1.

Consistent with theory (section 2.2), the vertical growth of layer 2 is only preferable when $\Delta \mathcal{E} > 0.04$, based on equations (12) and (42), and that growth rate increases with $\Delta \mathcal{E}$. Further, the growth of layer 2 occurs at the expense of that of layer 1; the size of layer 1 is a

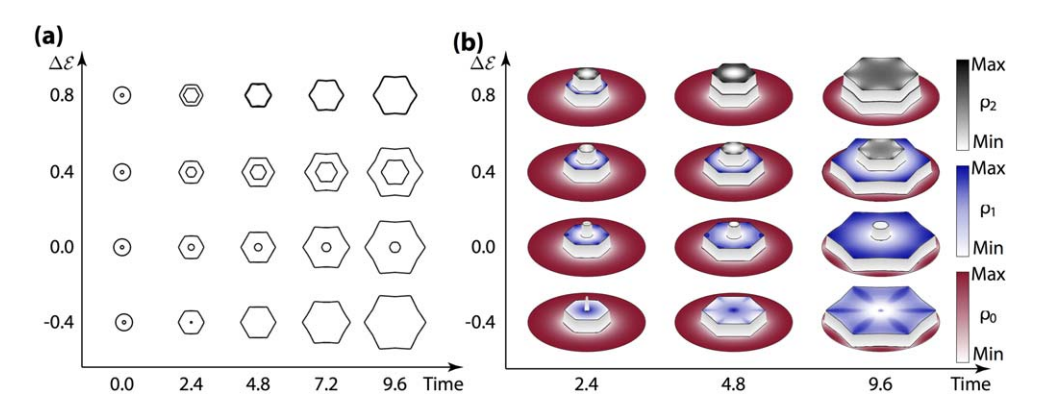


Figure E7. The effects of binding energy differences $\Delta \mathcal{E}$ for the time-dependent dynamics of layers 1 and 2 using six-fold symmetric anisotropic edge energies and kinetic coefficients. (a) Time evolution of the layer morphologies; (b) time evolution of the adatom concentrations on the layers. Compared to the quasi-steady case shown in figure E6, layer 1 grows more slowly but layer 2 grows more rapidly. In fact, layer 2 grows even when $\Delta \mathcal{E} = 0$, in contrast to the quasi-steady case where layer 2 shrinks when $\Delta \mathcal{E} = 0$.

decreasing function of $\Delta \mathcal{E}$. In all the cases, layer 1 is nearly faceted at early times, and develops negative curvatures at late times as layer 1 increases in size. Similar morphologies are observed for layer 2 with negative curvatures occurring when layer 2 is large enough (e.g. $\Delta \mathcal{E} = 0.8$).

For comparison, the morphologies for six-fold anisotropy obtained from the fully time-dependent dynamics are shown in E7. Compared to the quasi-steady case, we observe that the growth of layer 1 is significantly slower but that layer 2 actually grows more rapidly. Further, layer 2 grows even when $\Delta \mathcal{E} = 0$. This reflects the fact that vertical growth is more favorable when the growth rate of layer 1 is decreased, which is suggested by the theory in section 2.2.

In figures E8(a) and (b), the morphologies and adatom concentrations are shown, respectively, for three-fold anisotropic layers using the fully time-dependent dynamics. Qualitatively, the results are similar to the six-fold case in figure E7 although we observe that negative curvature occurs first in layer 2 before being manifest in layer 1.

4.4.2. Edge energy, surface diffusion and flux. In figure E9(a), we show the effects of edge energy γ on the growth of the layers in the fully time-dependent case. In both six-fold and three-fold anisotropies, we see that the growth rate of layer 2 decreases as we increase γ , and the layer 2 even shrinks when γ is large enough ($\gamma = 0.16$ or larger). The size of layer 1 is also decreased and the layer morphologies are smoother and the negative curvature on the layers disappears as γ is increased.

As seen in figure E9(b), surface diffusion also decreases the sizes of layer 2 and smoothens the layer corners although the negative curvature of the layers remains. In the six-fold anisotropic case, layer 1 is also decreased in size as β increases while in the three-fold anisotropic case, layer 1 is actually a little larger due to the decreased curvature at the vertices.

Next, we examine the effects of the adatom flux F_0 on the layer dynamics. As shown in figure E9(c), decreasing the supply of adatoms on the substrate (F_0) benefits the growth of second layer, which agrees with reported experimental observations for vertical growth of 2D

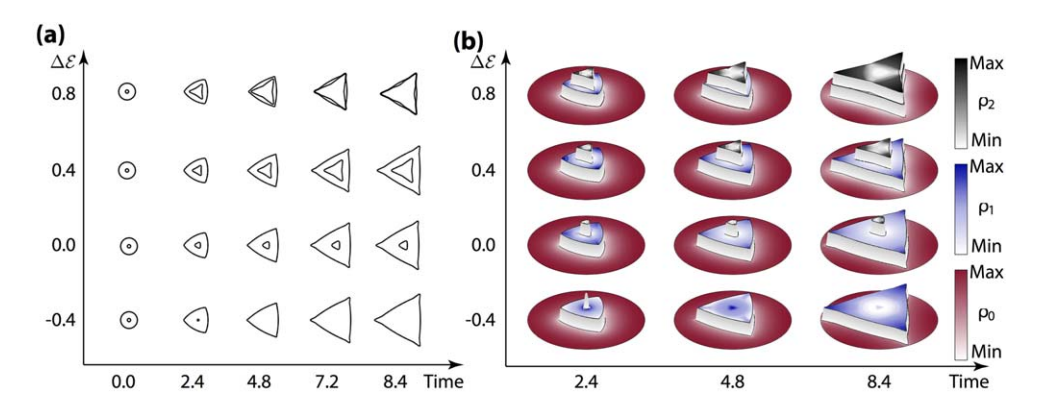


Figure E8. The effects of binding energy differences $\Delta \mathcal{E}$ for the time-dependent dynamics of layers 1 and 2 using three-fold symmetric anisotropic edge energies and kinetic coefficients. (a) Time evolution of the layer morphologies; (b) time evolution of the adatom concentrations on the layers. Qualitatively the growth criterion for layer 2 growth is similar to that for the six-fold, fully time-dependent case shown in figure E7. Quantitatively, the layers grow more rapidly in the three-fold case. Further, the negative curvature of the sides is more pronounced on layer 2.

materials (e.g. [14]). Moreover, in the case of six-fold anisotropy, we see that both layers develop negative curvatures at small F_0 , but as F_0 is increased the shapes become more facetted. Similar features are observed in the three-fold anisotropic case, except when $F_0 = 100$, where kinks with negative curvature develop at the boundary of layer 1. This feature persists under mesh refinement and seems to be associated with deposition only occurring on the substrate. If adatoms are deposited on all the layers, then layer 1 is convex at an equivalent size.

4.4.3. Kinetic coefficients. In figure E10(a), the kinetic parameter k_2^- is varied from 0.5 to 4.0 for layers with six-fold anisotropies. As predicted by the theory in section 2.2, increasing k_2^- favors the growth of layer 2 at the expense of layer 1. Both layers acquire negative curvature as they grow. In figure E10(b), we take $k_1^+ = k_1^-$ and vary this value from 0.5 to 4.0. In this case, the growth of layer 2 is insensitive to these changes, which is surprising because theory suggests that increasing k_1^+ increases layer 2 growth (equation (10)). The reason for the discrepancy is that a morphological instability occurs on layer 1 that accelerates its growth relative to that of layer 2. Because layer 1 grows faster, this reduces the number of adatoms available for layer 2 growth.

The growth of three-fold anisotropic layers subject to the same changes in the kinetic parameters shows somewhat different results. As seen in figures E11(a) and (b), increasing k_2^- and k_1^+ both favor the growth of layer 2. Further, when k_2^- is increased, only layer 2 acquires negative curvature while layer 1 remains convex, in contrast to the results found for six-fold anisotropy. In addition, when k_1^+ is increased, the morphological instability of layer 1 found in the six-fold case is not present in the three-fold case. Because of this layer 1 in the three-fold case does not grow as rapidly, relative to that of layer 2, which enables more adatoms to be available to drive the growth of layer 2.

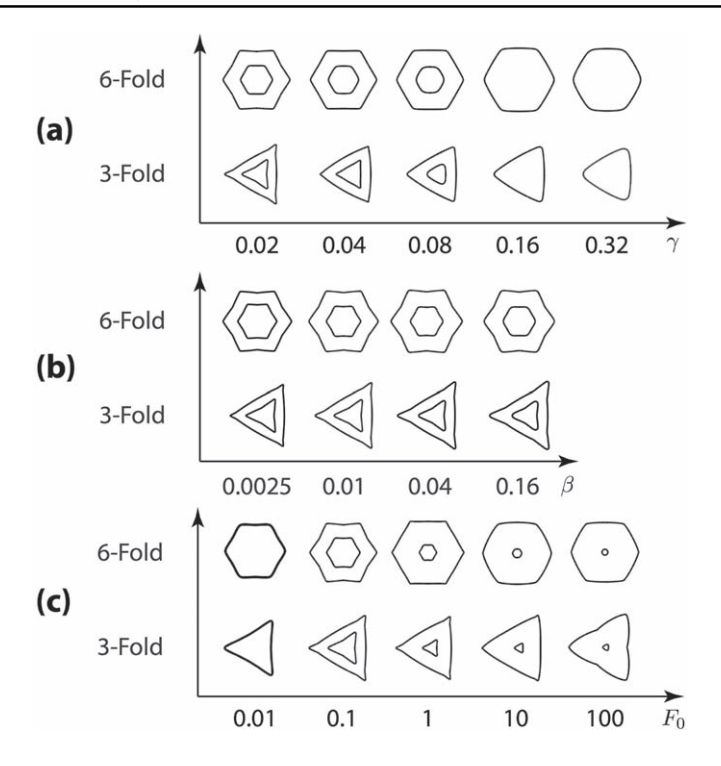


Figure E9. The morphologies of the six-fold and three-fold anisotropic layers at approximately the same sizes for different choices of edge energy strengths γ in (a), surface diffusion coefficients β in (b) and deposition fluxes F_0 in (c) All these parameters inhibit layer 2 growth. In (a) and (b), the six-fold and three-fold shapes are shown at times t=9.6 and t=8.4, respectively. In (c), the times shown for the six-fold case are $(F_0=0.01: t=60, F_0=0.1: t=9.6, F_0=1.0: t=2.8, F_0=10.0: t=0.8, F_0=10.0: t=0.8, F_0=1.0: t=2.25, F_0=10.0: t=0.65, F_0=10.0: t=0.15). See text for all the parameters.$

5. Conclusions

Epitaxial growth of 2D materials is a complex process, influenced by thermodynamic, kinetic and growth parameters, often leading to diverse and complex growth morphologies determined both by atomic-scale phenomena and by the elastic interactions of surface features and defects and transport of diffusing molecules over length scales of hundreds of nanometers. No single model can describe all the processes involved. In this paper, we derived a general continuum vdW-BCF model to describe the growth of vertically-stacked, arbitrarily-shaped multilayered 2D materials. The model accounted for (i) energy changes upon incorporation of adatoms into the growing 2D layers, (ii) kinetic barriers to attachment, (iii) distinct vdW interactions between the 2D layers and the substrate, (iv) energy penalties associated with the layer edges, and (v) the entropy of the adatoms. This is an extension of our previous work where we developed and analyzed an analogous model for faceted layers where the layer dynamics was much simpler [14]. The vdW-BCF system presented here represents a highly nonlinear free boundary problem.

We analyzed a nondimensional version of the vdW-BCF model and derived an analytic thermodynamic criterion for vertical growth of stacked 2D materials assuming the layers are

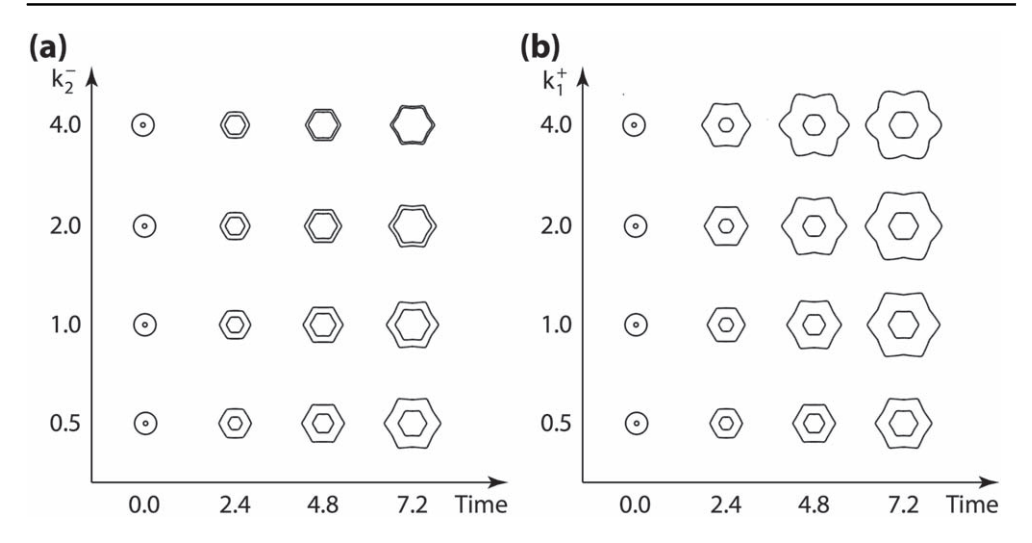


Figure E10. The effects of kinetic attachment coefficients on the dynamics of six-fold anisotropic layers 1 and 2. See text for parameters. In (a), only k_2^- is varied. In (b) $k_1^+ = k_1^-$ are varied together. The kinetic parameter k_2^- promotes layer 2 growth, as predicted by theory. The growth of layer 2 is insensitive to simultaneous changes in k_1^+ and k_1^- although layer 1, however, is significantly affected and undergoes a morphological instability.

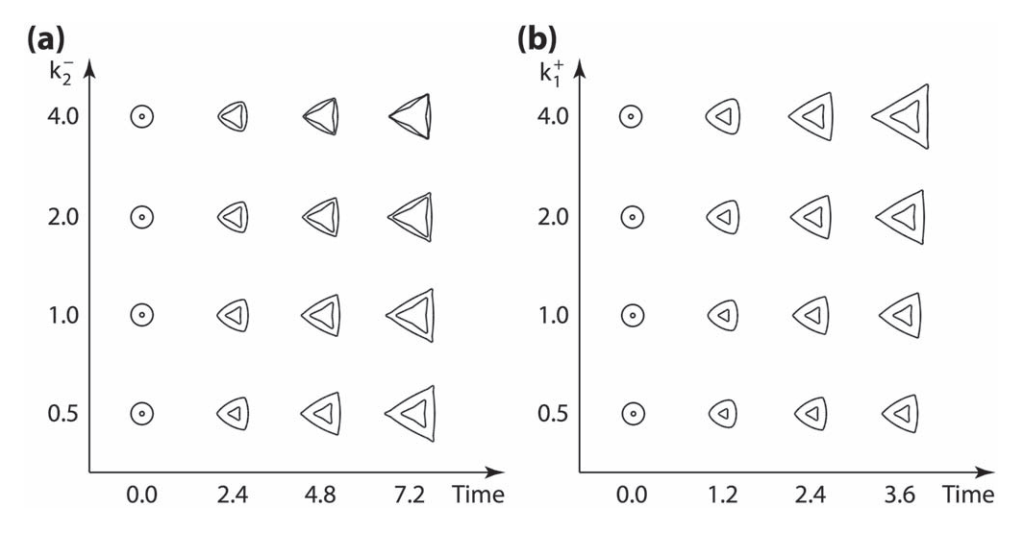


Figure E11. The effects of kinetic attachment coefficients on the dynamics of three-fold anisotropic layers 1 and 2. See text for parameters. In (a), only k_2^- is varied. In (b), $k_1^+ = k_1^-$ are varied together. In contrast to the six-fold case shown in figure E10, both kinetic parameters k_2^- and $k_1^+ = k_1^-$ promote the growth of layer 2 in the three-fold case. Further, the morphological instability observed in the six-fold case is not present in the three-fold case.

circular. To solve the system numerically, we used a second-order accurate phase-field/DDM that enabled us to solve the dynamic equations in a fixed regular domain. To discretize and solve the vdW-BCF-DDM reformulated system, we developed a second-order accurate

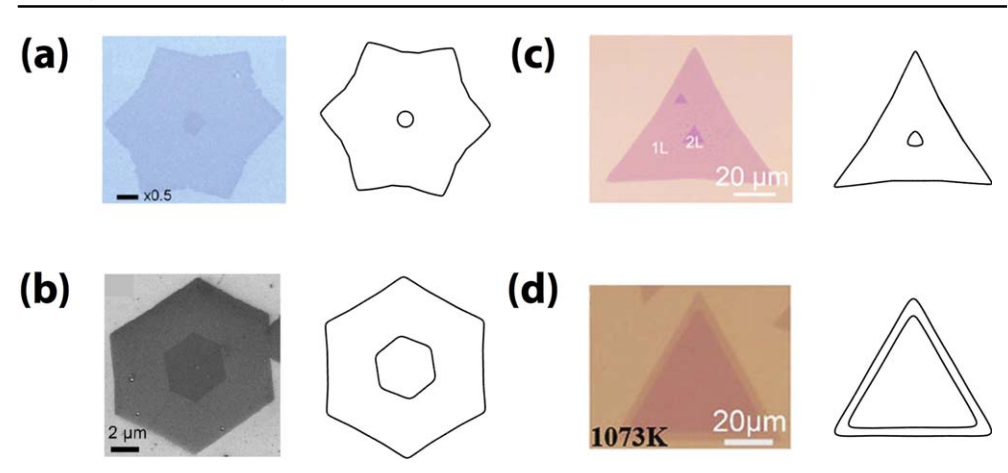


Figure E12. Experiments show a wide variety of bilayer morphologies of 2D materials, including layers with negative curvature, which our mathematical model is capable of reproducing. (a) Left: SEM image of bilayer graphene adapted from [10], with permission. Right: numerical simulation. (b) Left: SEM image of bilayer graphene with a twisted layer 2 adapted from [10], with permission. Right: numerical simulation with twist angle $\tilde{\theta}=10^{o}$ (see text). (c), (d) Left: optical images of TMD samples showing vertically-stacked bilayers of MoS₂ adapted from [14], with permission. Right: numerical simulations. See text for model parameters.

finite-difference/nonlinear multigrid method using adaptive, block-structured Cartesian mesh refinement. We demonstrated convergence of the numerical methods and investigated the effect of parameters on the layer growth and morphological evolution. While the conditions that favor vertical growth generally follow the thermodynamic criterion we derived for circular layers, the layer boundaries may develop significant curvature during growth and even morphological instabilities. These deviations from faceted shapes can alter the growth dynamics of the layers and can hinder or enhance vertical growth.

Experiments show a wide variety of layer morphologies, including layers with negative curvature, which our model is capable of reproducing. A small sample of experimental layer morphologies are shown in figure E12 together with our numerical simulations. Figure E12(a) shows a SEM image of bilayer graphene from [10] (left) that exhibits a star-shaped layer 1 and a nearly circular layer 2. The image on the right in figure E12(a) is a numerical simulation at time t=4 with the parameters from equation (42) except that $k_1^-=10$, $F_0=1$ and $\mathcal{E}_2=1.0$. Figure E12(b) shows a SEM image of bilayer graphene with a twisted layer 2 from [10] (left). This experiment was motivated by the observation that electronic structure of bilayer graphene can be altered by changing the relative twist angle, yielding a new class of low-dimensional carbon systems. To simulate twisted bilayer graphene, we modify the reference angle θ_0 of the kinetic coefficient $\xi_k(\theta)$ in equation (36). In particular, we set

$$\theta_0 = \begin{cases} \frac{\pi}{6} + \frac{2\pi}{360} \times \tilde{\theta} & \text{for } \varphi \in (1, 2], \\ \frac{\pi}{6} & \text{for } \varphi \in [0, 1], \end{cases}$$

$$(44)$$

where $\tilde{\theta}$ denotes the twist angle of layer 2. Here, we take $\tilde{\theta} = 10^{o}$ and all the other parameters are as in equation (42). The numerical result at time t = 8 is shown in the right figure of figure E12(b). Consistent with the experiment, layer 1 develops a hexagon shape with slight negative curvature while the twisted 2nd layer is nearly faceted. Figure E12(c) shows an

optical image of a vertically-stacked bilayer of MoS₂ from [14] (left) where layer 1 has a triangular shape with negatively curved sides and contains two smaller layer 2 triangles that are nearly faceted. The image on the right shows our numerical approximation at time t=3.84, which uses the parameters in equation (42) except with $k_1^{\pm}=3.0$, $k_2^{-}=6.0$, $\gamma_1=\gamma_2=0.02$, and $\mathcal{E}_2=1.0$. Finally, in figure E12(d), an optical image of a vertically-stacked bilayer of MoS₂ from [14](left) is shown where layer 2 nearly overlaps with layer 1 and both have shapes that are almost faceted. The figure on the right shows our numerical approximation at time t=2.8, which uses the parameters in equation (42) except with $\gamma_1=\gamma_2=0.04$, $F_0=0.012$, and $\mathcal{E}_2=5.0$.

Although we performed our study using a range of nondimensional parameters, atomistic and mesoscale models can be used to provide specific material parameters. For example, DFT simulations can provide estimates for vdW interaction energies as well as edge energies and kinetic barriers for attachment [12, 26, 14]. Incorporating such parameter estimates will be explored in future work.

Further, in this paper we have focused on single material homostructures due to perfect lattice matching and hence there are no interior strains. In the TMD family, one can go further and consider MoX_2/WX_2 heterostructures (M=Mo,W;X=S,Se,Te) without introducing lattice mismatch. However, taking full advantage of the device properties accessible through marriage of disparate 2D materials requires understanding the role of strain in the competition between vertical and in-plane lateral growth. We expect that strain-driven defect formation and stacking-site symmetry breaking will significantly modify the potential energy surface, affecting the thermodynamics of monolayer versus multilayer morphologies and the kinetics of adatom attachment. Such effects will also be considered in future work.

Acknowledgments

One of the authors (JL) thanks Dionisios Margetis for stimulating discussions. The authors gratefully acknowledge partial support from the National Science Foundation through Grants DMS-1522775 (JL), DMS-1522603 (VBS) and NSF CMMI-1727717 (VBS), as well as the Army Research Office through contract W911NF-16-1-0447.

Appendix A. Details of the derivation of the vdW-BCF model of verticallystacked multilayer growth

A.1. Mass conservation

We define the total mass to be:

$$M = \sum_{i=0}^{2} \int_{\Omega_{i}} \rho_{i} \, dA + \int_{\Omega_{1} \bigcup \Omega_{2}} \Omega_{s,1} \, dA + \int_{\Omega_{2}} \Omega_{s,2} \, dA, \tag{A.1}$$

where $\Omega_{s,i}$ are the concentrations of atomic sites in the layers (i = 1, 2). Then, mass conservation requires

$$\frac{\mathrm{d}M}{\mathrm{d}t} = \sum_{i=0}^{2} \left(\int_{\Omega_i} F_i \, \mathrm{d}A - \int_{\Omega_i} \tau_{d,i}^{-1} \rho_i \, \mathrm{d}A \right),\tag{A.2}$$

where F_i is the deposition flux on layer i and $\tau_{d,i}^{-1}$ are desorption rates. Combining these two equations and using the Reynolds transport theorem gives:

$$\frac{\mathrm{d}M}{\mathrm{d}t} = \sum_{i=0}^{2} \int_{\Omega_{i}} \partial_{t} \rho_{i} + \nabla \cdot (\rho_{i} \mathbf{v}_{i}) \mathrm{d}A + \int_{\Omega_{1} \cup \Omega_{2}} \nabla \cdot (\Omega_{s,1} \mathbf{v}_{1}) \, \mathrm{d}A \int_{\Omega_{2}} \nabla \cdot (\Omega_{s,2} \mathbf{v}_{2}) \, \mathrm{d}A, \tag{A.3}$$

where \mathbf{v}_i are the velocities of the adatoms on the layers and substrate. For simplicity, we assume that $\Omega_{s,i} = \Omega_s$. We also assume that the boundary of the substrate Γ_0 does not move. Therefore, combining equations (A.2) and (A.3) and using the divergence theorem we obtain

$$0 = \sum_{i=1}^{2} \int_{\Gamma_{i}} v_{i} (\rho_{i}^{+} - \rho_{i}^{-} + \Omega_{s}) dA + \sum_{i=0}^{2} \int_{\Omega_{i}} (\partial_{t} \rho_{i} - F_{i} + \tau_{d,i}^{-1} \rho_{i}) dA, \quad (A.4)$$

where $v_i = \mathbf{v} \cdot \mathbf{n}_{\Gamma_i}$ is the normal velocity of layer i, and $\rho_i^+ = \rho_i|_{\Gamma_i}$, $\rho_i^- = \rho_{i-1}|_{\Gamma_i}$ are the boundary conditions for the densities at the ith layer from the step up and down respectively. Next, assuming that

$$\partial_t \rho_i = -\nabla \cdot \mathbf{J}_i + F_i - \tau_{d,i}^{-1} \rho_i, \tag{A.5}$$

then the last term in equation (A.4) can be written as

$$\sum_{i=0}^{2} \int_{\Omega_{i}} (\partial_{t} \rho_{i} - F_{i} - \tau_{d,i}^{-1} \rho_{i}) = -\sum_{i=0}^{2} \int_{\Omega_{i}} \nabla \cdot \mathbf{J}_{i} \, dA$$

$$= -\int_{\Gamma_{2}} (J_{2}^{+} - J_{2}^{-}) dS - \int_{\Gamma_{i}} (J_{1}^{+} - J_{1}^{-}) dS, \tag{A.6}$$

where J_i^{\pm} (for i=1, 2) denote the fluxes at the *i*th layer from a step up and down, respectively, with

$$\mathbf{J}_2 \cdot \mathbf{n}_{\Gamma_2} = J_2^+, \qquad \mathbf{J}_1 \cdot \mathbf{n}_{\Gamma} = J_1^+, \tag{A.7}$$

$$\mathbf{J}_1 \cdot \mathbf{n}_{\Gamma_2} = J_2^-, \qquad \mathbf{J}_0 \cdot \mathbf{n}_{\Gamma_1} = J_1^-, \tag{A.8}$$

and we have assumed that there is no flux at the substrate boundary: $\mathbf{J}_0 \cdot \mathbf{n}_{\partial \Gamma_0} = J_0 = 0$. Further, the boundary conditions for equation (A.5) on Γ_i are taken to be

$$q_i^+ = J_i^+ - \rho_i^+ v_i, \tag{A.9}$$

$$q_i^- = -J_i^- + \rho_i^- v_i. (A.10)$$

Substituting (A.6) and (A.9), (A.10), into (A.4), we obtain

$$\sum_{i=1}^{2} \int_{\Gamma_{i}} (v_{i} \Omega_{s} - (q_{i}^{+} + q_{i}^{-})) dS = 0.$$
(A.11)

In order to satisfy mass conservation, we then have

$$v_{1} = \frac{1}{\Omega_{s}} (q_{1}^{+} + q_{1}^{-} - \partial_{s} \mathcal{J}_{1}), \tag{A.12}$$

$$v_2 = \frac{1}{\Omega_s} (q_2^+ + q_2^- - \partial_s \mathcal{J}_2), \tag{A.13}$$

where ∂_s denotes the arclength derivative and \mathcal{J}_i represents surface fluxes (e.g. arising from the diffusion of adatoms along the layer edges). To obtain constitutive laws for the fluxes q_i , \mathbf{J}_i and \mathcal{J}_i , we require that the system dissipates the free energy when the deposition flux $F_i = 0$ and desorption coefficient $\tau_{d,i}^{-1} = 0$.

A.2. Free energy dissipation

Taking the time derivative of the free energy E from equation (1) and using the Reynolds transport theorem, we obtain

$$\frac{\mathrm{d}E}{\mathrm{d}t} = \sum_{i=1}^{2} \left(-\int_{\Omega_{i}} \nabla \cdot (\mathcal{E}_{i} \mathbf{v}_{i}) \, \mathrm{d}A + \int_{\Gamma_{i}} \tilde{\gamma}_{i} v_{i} \kappa_{i} \, \mathrm{d}S \right)
+ k_{B} T \sum_{i=0}^{2} \int_{\Omega_{i}} \left(\partial_{t} \rho_{i} \left(\ln \frac{\rho_{i}}{\rho_{\text{ref}}} - \ln \left(1 - \frac{\rho_{i}}{\rho_{\text{ref}}} \right) \right) \right) \, \mathrm{d}A
+ k_{B} T \rho_{ref} \sum_{i=0}^{2} \int_{\Omega_{i}} \nabla \cdot \left(\mathbf{v}_{i} \left(\frac{\rho_{i}}{\rho_{\text{ref}}} \ln \frac{\rho_{i}}{\rho_{\text{ref}}} + \left(1 - \frac{\rho_{i}}{\rho_{\text{ref}}} \right) \ln \left(1 - \frac{\rho_{i}}{\rho_{\text{ref}}} \right) \right) \right) \, \mathrm{d}A,$$
(A.14)

where $\tilde{\gamma}_i = \gamma_i(\theta) + \gamma_i''(\theta)$ and the primes denote derivatives with respect to θ , the normal angle (e.g. angle that the normal vector makes with the *x*-axis). Defining the free energy density f and the chemical potential μ to be

$$f(\rho) = k_{\rm B} T \left(\frac{\rho}{\rho_{\rm ref}} \ln \frac{\rho}{\rho_{\rm ref}} + \left(1 - \frac{\rho}{\rho_{\rm ref}} \right) \ln \left(1 - \frac{\rho}{\rho_{\rm ref}} \right) \right), \tag{A.15}$$

$$\mu(\rho) = \frac{\partial f}{\partial \rho} = k_B T \left(\ln \frac{\rho}{\rho_{\text{ref}}} - \ln \left(1 - \frac{\rho}{\rho_{\text{ref}}} \right) \right)$$
 (A.16)

and applying the divergence theorem, we obtain

$$\frac{\mathrm{d}E}{\mathrm{d}t} = \int_{\Gamma_2} v_2(-\mathcal{E}_2 + \mathcal{E}_1 + \tilde{\gamma}_2 \kappa_2) \mathrm{d}S + \int_{\Gamma_1} v_1(-\mathcal{E}_1 + \tilde{\gamma}_1 \kappa_1) \mathrm{d}S + \sum_{i=0}^2 \int_{\Omega_i} \mu_i \partial_t \rho_i \, \mathrm{d}A
+ \sum_{i=1}^2 \int_{\Gamma_i} v_i (f(\rho_i^+) - f(\rho_i^-) \mathrm{d}S,$$
(A.17)

where $\mu_i = \mu(\rho_i)$. Next, using equation (A.5) in equation (A.17) we obtain

$$\frac{\mathrm{d}E}{\mathrm{d}t} = \int_{\Gamma_{2}} v_{2}(-\mathcal{E}_{2} + \mathcal{E}_{1} + \tilde{\gamma}_{2}\kappa_{2} + f(\rho_{2}^{+}) - f(\rho_{2}^{-}) \,\mathrm{d}S
+ \int_{\Gamma_{2}} v_{1}(-\mathcal{E}_{1} + \tilde{\gamma}_{1}\kappa_{1} + f(\rho_{1}^{+}) - f(\rho_{1}^{-}) \,\mathrm{d}S
\times \sum_{i=0}^{2} \left(-\int_{\Omega_{i}} \mu_{i} \nabla \cdot \mathbf{J}_{i} \,\mathrm{d}A + \int_{\Omega_{i}} \mu_{i} (F_{i} - \tau_{d,i}^{-1} \rho_{i}) \,\mathrm{d}A\right).$$
(A.18)

Integrating by parts and using the divergence theorem, we obtain

$$\frac{dE}{dt} = \int_{\Gamma_{2}} v_{2}(-\mathcal{E}_{2} + \mathcal{E}_{1} + \tilde{\gamma}_{2}\kappa_{2} + f(\rho_{2}^{+}) - f(\rho_{2}^{-}) - (\mu_{2}^{+}J_{2}^{+} - \mu_{2}^{-}J_{2}^{-}) dS
+ \int_{\Gamma_{1}} v_{1}(-\mathcal{E}_{1} + \tilde{\gamma}_{1}\kappa_{1} + f(\rho_{1}^{+}) - f(\rho_{1}^{-}) - (\mu_{1}^{+}J_{1}^{+} - \mu_{1}^{-}J_{1}^{-}) dS
+ \sum_{i=0}^{2} \left(\int_{\Omega_{i}} \mathbf{J}_{i} \cdot \nabla \mu_{i} dA + \int_{\Omega_{i}} \mu_{i}(F_{i} - \tau_{d,i}^{-1}\rho_{i}) dA \right),$$
(A.19)

where we have defined $\mu_i^{\pm} = \mu(\rho_i^{\pm})$. See the previous subsection for the definitions of ρ_i^{\pm} and J_i^{\pm} . Using equations (A.9), (A.10), (A.12) and (A.13) in equation (A.19) we obtain:

$$\begin{split} \frac{\mathrm{d}E}{\mathrm{d}t} &= \int_{\Gamma_{2}} q_{2}^{+} (\rho_{2}^{\mathrm{BC}} - \mu_{2}^{+}) + q_{2}^{-} (\rho_{2}^{\mathrm{BC}} - \mu_{2}^{-}) + \mathcal{J}_{2} \partial_{s} \rho_{2}^{\mathrm{BC}} \, \mathrm{d}S \\ &+ \int_{\Gamma_{1}} q_{1}^{+} (\rho_{1}^{\mathrm{BC}} - \mu_{1}^{+}) + q_{1}^{-} (\rho_{1}^{\mathrm{BC}} - \mu_{1}^{-}) + \mathcal{J}_{1} \partial_{s} \rho_{1}^{\mathrm{BC}} \, \mathrm{d}S \\ &+ \sum_{i=0}^{2} \left(\int_{\Omega_{i}} \mathbf{J}_{i} \cdot \nabla \mu_{i} \, \mathrm{d}A + \int_{\Omega_{i}} \mu_{i} (F_{i} - \tau_{d,i}^{-1} \rho_{i}) \, \mathrm{d}A \right), \end{split} \tag{A.20}$$

where we have integrated by parts on the edges Γ_1 and Γ_2 and defined

$$\rho_2^{\text{BC}} = \frac{1}{\Omega_s} (-\mathcal{E}_2 + \mathcal{E}_1 + \tilde{\gamma}_2 \kappa_2 + L_f(\rho_2^+) - L_f(\rho_2^-)), \tag{A.21}$$

$$\rho_1^{\text{BC}} = \frac{1}{\Omega_s} (-\mathcal{E}_1 + \tilde{\gamma}_1 \kappa_1 + L_f(\rho_1^+) - L_f(\rho_1^-)), \tag{A.22}$$

where

$$L_f(\rho_i^{\pm}) = f(\rho_i^{\pm}) - \rho_i^{\pm} \mu_i^{\pm} = k_{\rm B} T \rho_{ref} \ln \left(1 - \frac{\rho_i^{\pm}}{\rho_{\rm ref}} \right). \tag{A.23}$$

Hence, to have energy dissipation (in the absence of flux and desorption), we may take the constitutive relations for the fluxes:

$$\mathbf{J}_i = -D_i \nabla \mu_i, \tag{A.24}$$

$$\mathcal{J}_2 = -\beta_2 \partial_s \rho_2^{\text{BC}},\tag{A.25}$$

$$\mathcal{J}_1 = -\beta_1 \partial_s \rho_1^{\text{BC}},\tag{A.26}$$

where the β_i are related to the mobility of an edge atom along a curved step, and the (linear) kinetic boundary conditions:

$$q_2^{\pm} = k_2^{\pm}(\mu_2^{\pm} - \rho_2^{\text{BC}}),$$
 (A.27)

$$q_1^{\pm} = k_1^{\pm}(\mu_1^{\pm} - \rho_1^{\text{BC}}),$$
 (A.28)

where k_i^{\pm} are kinetic attachment coefficients.

A.3. Model simplification

Since $\rho_i^+ \approx \rho_i^-$ and $\rho_i^+ - \rho_i^- \ll \Omega_s$, we can neglect the terms $\frac{1}{\Omega_s}(L_f(\rho_i^+) - L_f(\rho_i^-))$ in ρ_i^{BC} . Therefore ρ_i^{BC} are approximated by

$$\rho_2^{\text{BC}} = \frac{1}{\Omega_s} (-\mathcal{E}_2 + \mathcal{E}_1 + \tilde{\gamma}_2 \kappa_2), \tag{A.29}$$

$$\rho_1^{\text{BC}} = \frac{1}{\Omega_c} (-\mathcal{E}_1 + \tilde{\gamma}_1 \kappa_1). \tag{A.30}$$

Further, μ_i^{\pm} can be approximated as

$$\mu_i = k_B T \left(\ln \frac{\rho_i}{\rho_{\text{ref}}} - \ln \left(1 - \frac{\rho_i}{\rho_{\text{ref}}} \right) \right) \approx 4k_B T \left(\frac{\rho_i}{\rho_{\text{ref}}} - \frac{1}{2} \right). \tag{A.31}$$

We further neglect the effects of anisotropy in the surface fluxes (e.g. we assume that the edge energy anisotropy is small $\tilde{\gamma}_i(\theta) \approx \tilde{\gamma}_i$), although we keep the effects of anisotropy in the kinetic coefficients and in ρ_i^{BC} . Surface diffusion anisotropy will be considered in future work. It follows that the diffusional and surface fluxes can be approximated by

$$\mathbf{J}_{i} \approx -\tilde{D}_{i} \nabla \rho_{i}, \quad \mathcal{J}_{i} = -\tilde{\beta}_{i} \partial_{s} \kappa_{i},$$
 (A.32)

where $\tilde{D}_i = \frac{4D_i k_B T}{\rho_{\rm ref}^2}$ and $\tilde{\beta}_i = \frac{\beta_i \tilde{\gamma}_i}{\Omega_s}$ the velocities can be approximated as

$$v_1 = \frac{1}{\Omega_s} (q_1^+ + q_1^- + \tilde{\beta}_1 \partial_{ss} \kappa_1),$$
 (A.33)

$$v_2 = \frac{1}{\Omega_s} (q_2^+ + q_2^- + \tilde{\beta}_2 \partial_{ss} \kappa_2), \tag{A.34}$$

and the kinetic boundary conditions can be approximated as

$$q_2^+ = \tilde{k}_2^+ \left(\rho_2^+ - \frac{1}{\tilde{\Omega}_s} (-\tilde{\mathcal{E}}_2 + \tilde{\mathcal{E}}_1 + \tilde{\gamma}_2 \kappa_2) \right), \tag{A.35}$$

$$q_2^- = \tilde{k}_2^- \left(\rho_2^- - \frac{1}{\tilde{\Omega}_s} (-\tilde{\mathcal{E}}_2 + \tilde{\mathcal{E}}_1 + \tilde{\gamma}_2 \kappa_2) \right), \tag{A.36}$$

$$q_1^+ = \tilde{k}_1^+ \left(\rho_1^+ - \frac{1}{\tilde{\Omega}_c} (-\tilde{\mathcal{E}}_1 + \tilde{\gamma}_1 \kappa_1) \right), \tag{A.37}$$

$$q_{\rm l}^- = \tilde{k}_{\rm l}^- \left(\rho_{\rm l}^- - \frac{1}{\tilde{\Omega}_s} (-\tilde{\mathcal{E}}_{\rm l} + \tilde{\gamma}_{\rm l} \kappa_{\rm l}) \right), \tag{A.38}$$

where $\tilde{k}_i^{\pm} = \frac{4k_i^{\pm}k_BT}{\rho_{ref}}$, $\tilde{\Omega}_s = \frac{\Omega_s 4k_BT}{\rho_{ref}}$, and $\tilde{\mathcal{E}}_i = \mathcal{E}_i - \frac{\rho_{ref}}{2}\tilde{\Omega}_s$. Finally, equation (A.5) can be approximated by

$$\partial_t \rho_i = \tilde{D}_i \Delta \rho_i + F_i - \tau_{d,i}^{-1} \tag{A.39}$$

A.4. Nondimensionalization

Let $\rho_{\rm ref}=\Omega_s$, \mathcal{L} be the characteristic size of layer 1 and take the time scale to be $\mathcal{T}=\mathcal{L}^2\Omega_s/(4Dk_{\rm B}T)$, where D is a characteristic diffusion constant. Define the nondimensional density $\rho_i'=\rho_i/\Omega_s$ and the nondimensional flux $F_i'=TF_i/\Omega_s$, where the nondimensional desorption coefficient is $\tau_{d,i}'=\tau_{d,i}/T$. Then, the nondimensional adatom density equation (A.39) becomes:

$$\partial_{t'}\rho_i' = D_i'\Delta'\rho_i' + F_i' - (\tau_{d,i}')^{-1}\rho_i', \tag{A.40}$$

where $D_i' = D_i/D$ is the nondimensional diffusion coefficient. The kinetic boundary conditions become

$$q_2'^{+} = k_2'^{+}(\rho_2' - \rho^*(-\mathcal{E}_2' + \mathcal{E}_1' + \tilde{\gamma}_2'\kappa_2'), \tag{A.41}$$

$$q_2^{\prime -} = -k_2^{\prime -} (\rho_1^{\prime} - \rho^* (-\mathcal{E}_2^{\prime} + \mathcal{E}_1^{\prime} + \tilde{\gamma}_2^{\prime} \kappa_2^{\prime}), \tag{A.42}$$

$$q_1'^{+} = k_1'^{+}(\rho_1' - \rho^*(-\mathcal{E}_1' + \tilde{\gamma}_1'\kappa_1'), \tag{A.43}$$

$$q_1'^- = -k_1'^- (\rho_0' - \rho^* (-\mathcal{E}_1' + \tilde{\gamma}_1' \kappa_1'). \tag{A.44}$$

where

$$q_{i}^{\prime\pm} = \frac{\mathcal{L}\rho_{\text{ref}}}{4Dk_{\text{B}}T}q_{i}^{\pm}, \quad k_{i}^{\prime\pm} = k_{1,2}^{\pm}\frac{\mathcal{L}\rho_{\text{ref}}}{D}, \quad \rho^{*} = \frac{\mathcal{E}}{4k_{\text{B}}T}, \quad \mathcal{E}_{i}^{\prime} = \mathcal{E}_{i}/\mathcal{E} - \frac{1}{2\rho^{*}}, \quad \tilde{\gamma}_{i}^{\prime} = \tilde{\gamma}_{i}/(\mathcal{E}\mathcal{L}),$$
(A.45)

and \mathcal{E} is a characteristic value of the binding energies. Finally, the nondimensional velocities are:

$$v_1' = q_1'^+ + q_1'^- + \beta_1' \partial_{s's'} \kappa_1', \tag{A.46}$$

$$v_2' = q_2'^+ + q_2'^- + \beta_2' \partial_{s's'} \kappa_2', \tag{A.47}$$

where $\beta_i' = \frac{\beta_i \bar{\gamma_i}}{4Dk_BT\mathcal{L}^2}$ are nondimensional edge diffusion coefficients. Dropping the primes, this is the system given in section 2.1.

A.5. The vdW-BCF model equations for an arbitrary number of vertically-stacked layers

One can extend the vdW-BCF model derived in the previous sections to describe the dynamics of an arbitrary number of layers. The resulting (nondimensional) system is

$$\partial_t \rho_i = D_i \Delta \rho_i + F_i - \tau_d^{-1} \rho_i \quad \text{in } \Omega_i, \quad i = 0, 1, \dots n, \tag{A.48}$$

where n is the number of layers. The boundary conditions at the boundary of the first layer with the substrate, Γ_1 , are given as

$$q_1^+ = -D_1 \nabla \rho_1 \cdot \mathbf{n}_{\Gamma_1} - \rho_1 |_{\Gamma_1} = k_1^+ (\rho_1 - \rho^* (-\mathcal{E}_1 + \gamma_1 \kappa_1), \tag{A.49}$$

$$q_{1}^{-} = D_{0} \nabla \rho_{0} \cdot \mathbf{n}_{\Gamma_{1}} + \rho_{0}|_{\Gamma_{1}} = k_{1}^{-} (\rho_{0} - \rho^{*} (-\mathcal{E}_{1} + \gamma_{1} \kappa_{1}), \tag{A.50}$$

and for all the layer boundaries (e.g. steps) Γ_i (for i = 2, ..., n) are:

$$q_i^+ = -D_i \nabla \rho_i \cdot \mathbf{n}_{\Gamma_i} - \rho_i|_{\Gamma_i} = k_i^+ (\rho_i - \rho^* (-\mathcal{E}_i + \mathcal{E}_{i-1} + \gamma_i \kappa_i), \tag{A.51}$$

$$q_{i}^{-} = D_{i-1} \nabla \rho_{i-1} \cdot \mathbf{n}_{\Gamma_{i}} + \rho_{i-1}|_{\Gamma_{i}} = k_{i}^{-} (\rho_{i-1} - \rho^{*} (-\mathcal{E}_{i} + \mathcal{E}_{i-1} + \gamma_{i} \kappa_{i}), \tag{A.52}$$

where γ_i denotes the step stiffness and κ_i is the curvature of the *i*th step Γ_i , for i = 1, 2...n. The normal velocity of each step Γ_i is given by

$$v_i = q_i^+ + q_i^- + \beta \partial_s^2 \kappa_i. \tag{A.53}$$

Appendix B. Details of the derivation of radial solutions to the vdW-BCF model

We now derive the analytic solutions $\rho_i(r, t)$ in the quasi-steady state limit. That is, we drop the time derivatives in the adatom diffusion equations. We first rewrite equation (2) as

$$-\frac{D_i}{r}\partial_r(r\partial_r\rho_i) = F_i,\tag{B.1}$$

where we have also neglected desorption and taken $\tau_{d,i}^{-1} = 0$. Integrating twice we obtain:

$$\rho_i = -\frac{F_i}{4D_i}r^2 + A_i \ln(r) + B_i, \quad \text{for } i = 0, 1, 2,$$
(B.2)

where A_i and B_i are unknown constants.

For $r < R_2(t)$, the solution in equation (B.2) satisfies the following boundary conditions:

$$\rho_2$$
 is continuous, at $r = 0$, (B.3)

$$-D_2 \partial_r \rho_2 = k_2^+ \left[\rho_2 - \rho^* \left(-\mathcal{E}_2 + \mathcal{E}_1 + \frac{\gamma_2}{R_2} \right) \right], \quad \text{at } r = R_2.$$
 (B.4)

We then obtain

$$A_2 = 0, \quad B_2 = \frac{F_2 R_2^2}{4D_2} + \frac{F_2 R_2}{2k_2^+} + \rho^* \left(-\mathcal{E}_2 + \mathcal{E}_1 + \frac{\gamma_2}{R_2} \right).$$
 (B.5)

For $R_2 < r < R_1$, the solution in equation (B.2) satisfies

$$D_1 \partial_r \rho_1 = k_2^- \left[\rho_1 - \rho^* \left(-\mathcal{E}_2 + \mathcal{E}_1 + \frac{\gamma_2}{R_2} \right) \right], \quad \text{at } r = R_2,$$
 (B.6)

$$-D_1 \partial_r \rho_1 = k_1^+ \left[\rho_1 - \rho^* \left(-\mathcal{E}_1 + \frac{\gamma_1}{R_1} \right) \right], \quad \text{at } r = R_1.$$
 (B.7)

At $r = R_2$, we obtain

$$B_{1} = \frac{F_{1}R_{2}^{2}}{4D_{1}} - A_{1} \ln R_{2} + \frac{D_{1}}{k_{2}^{-}} \left(-\frac{F_{1}R_{2}}{2D_{1}} + \frac{A_{1}}{R_{2}} \right) + \rho^{*} \left(-\mathcal{E}_{2} + \mathcal{E}_{1} + \frac{\gamma_{2}}{R_{2}} \right).$$
(B.8)

At $r = R_1$, we obtain

$$B_1 = \frac{F_1 R_1^2}{4D_1} - A_1 \ln R_1 - \frac{D_1}{k_1^+} \left(-\frac{F_1 R_1}{2D_1} + \frac{A_1}{R_1} \right) + \rho^* \left(-\mathcal{E}_1 + \frac{\gamma_1}{R_1} \right), \tag{B.9}$$

such that

$$A_{1} = \frac{\frac{F_{1}}{4D_{1}}(R_{2}^{2} - R_{1}^{2}) + \rho^{*}\left(-\mathcal{E}_{2} + \mathcal{E}_{1} + \frac{\gamma_{2}}{R_{2}}\right) - \frac{F_{1}R_{1}}{2k_{1}^{+}} - \frac{F_{1}R_{2}}{2k_{2}^{-}} - \rho^{*}\left(-\mathcal{E}_{1} + \frac{\gamma_{1}}{R_{1}}\right)}{\left(\ln\frac{R_{2}}{R_{1}} - \frac{D_{1}}{k_{2}^{-}R_{2}} - \frac{D_{1}}{k_{1}^{+}R_{1}}\right)}.$$
 (B.10)

For $R_1 < r < R_{\infty}$, the solution in equation (B.2) satisfies

$$D_0 \partial_r \rho_0 = k_1^- \left(\rho_0 - \rho^* \left(-\mathcal{E}_1 + \frac{\gamma_1}{R_1} \right) \right), \quad \text{at } r = R_1,$$
 (B.11)

$$\partial_r \rho_0 = 0$$
, at $r = R_\infty$. (B.12)

At $r = R_1$, we obtain

$$-\frac{F_0 R_1^2}{4D_0} + A_0 \ln R_1 + B_0 - \frac{D_0}{k_1^-} \left(-\frac{F_0 R_1}{2D_0} + \frac{A_0}{R_1} \right) = \rho^* \left(-\mathcal{E}_1 + \frac{\gamma_1}{R_1} \right). \tag{B.13}$$

At $r = R_0$, we obtain

$$A_0 = \frac{F_0}{2D_0} R_0^2. ag{B.14}$$

such that

$$B_0 = \frac{F_0 R_1^2}{4D_0} - \frac{F_0 R_0^2}{2D_0} \ln R_1 - \frac{F_0 R_1}{2k_1^-} + \frac{F_0 R_0^2}{2k_0^- R_1} + \rho^* \left(-\mathcal{E}_1 + \frac{\gamma_1}{R_1} \right). \tag{B.15}$$

Summarizing, we obtain the analytic solution

$$\rho_2 = -\frac{F_2}{4D_2}r^2 + A_2 \ln(r) + B_2, \qquad x < R_2,
\rho_1 = -\frac{F_1}{4D_1}r^2 + A_1 \ln(r) + B_1, \qquad R_2 < x < R_1,
\rho_0 = -\frac{F_0}{4D_0}r^2 + A_0 \ln(r) + B_0, \qquad R_1 < x,$$
(B.16)

where

$$A_2 = 0,$$

$$\begin{split} B_2 &= \frac{F_2 R_2^2}{4D_2} + \frac{F_2 R_2}{2k_2^+} + \rho^* \bigg(-\mathcal{E}_2 + \mathcal{E}_1 + \frac{\gamma_2}{R_2} \bigg), \\ A_1 &= \frac{\frac{F_1}{4D_1} (R_2^2 - R_1^2) + \rho^* \bigg(-\mathcal{E}_2 + \mathcal{E}_1 + \frac{\gamma_2}{R_2} \bigg) - \frac{F_1 R_1}{2k_1^+} - \frac{F_1 R_2}{2k_2^-} - \rho^* \bigg(-\mathcal{E}_1 + \frac{\gamma_1}{R_1} \bigg)}{\bigg(\ln \frac{R_2}{R_1} - \frac{D_1}{k_2^- R_2} - \frac{D_1}{k_1^+ R_1} \bigg)}, \\ B_1 &= \frac{F_1 R_1^2}{4D_1} - A_1 \ln R_1 - \frac{D_1}{k_1^+} \bigg(-\frac{F_1 R_1}{2D_1} + \frac{A_1}{R_1} \bigg) + \rho^* \bigg(-\mathcal{E}_1 + \frac{\gamma_1}{R_1} \bigg), \\ A_0 &= \frac{F_0}{2D_0} R_0^2, \\ B_0 &= \frac{F_0 R_1^2}{4D_0} - \frac{F_0 R_0^2}{2D_0} \ln R_1 - \frac{F_0 R_1}{2k_1^-} + \frac{F_0 R_0^2}{2k_0 R_1} + \rho^* \bigg(-\mathcal{E}_1 + \frac{\gamma_1}{R_1} \bigg). \end{split}$$

The corresponding velocities of the layer boundaries are

$$v_2 = -(D_2 \partial_r \rho_2 - D_1 \partial_r \rho_1)|_{r=R_2} = \frac{R_2 (F_2 - F_1)}{2} + \frac{D_1 A_1}{R_2},$$
(B.17)

$$v_1 = -(D_1 \partial_r \rho_1 - D_0 \partial_r \rho_0)|_{r=R_1} = \frac{R_1 (F_1 - F_0)}{2} + \frac{D_0 A_0 - D_1 A_1}{R_1}.$$
 (B.18)

Appendix C. The diffuse domain method: details and asymptotic analysis

For simplicity, consider the problem with a single layer:

$$\partial_t \rho_i = D_i \Delta \rho_i + F_i - \tau^{-1} \rho_i, \quad \text{in } \Omega_i(t),$$
 (C.1)

where i = 0, 1 denote the substrate and layer, respectively. The kinetic boundary conditions are:

$$q_1^+ = -D_1 \nabla \rho_1 \cdot \mathbf{n}_1 - \rho_1 v_1 = k_1^+ (\rho_1 - \rho^* (-\mathcal{E}_1 + \tilde{\gamma}_1 \kappa)), \tag{C.2}$$

$$q_1^- = D_0 \nabla \rho_0 \cdot \mathbf{n}_1 + \rho_0 v_1 = k_1^- (\rho_0 - \rho^* (-\mathcal{E}_1 + \tilde{\gamma}_1 \kappa))$$
 (C.3)

with the normal velocity of $\Gamma_1(t) = \partial \Omega_1(t)$ given by

$$v_1 = q_1^+ + q_1^- + \beta \partial_s^2 \kappa. \tag{C.4}$$

In the above, κ is the curvature of Γ_1 .

Next, following [21, 17], we can reformulate equations (C.1)–(C.3) as

$$\partial_t(\varphi \rho_1^{\epsilon}) = \nabla \cdot (D_1 \varphi \nabla \rho_1^{\epsilon}) + \varphi (F_1 - \tau^{-1} \rho_1^{\epsilon}) - k_1^+ |\nabla \varphi| (\rho_1^{\epsilon} - g), \tag{C.5}$$

$$\partial_t(\varphi^c \rho_0^{\epsilon}) = \nabla \cdot (D_0 \varphi^c \nabla \rho_0^{\epsilon}) + \varphi^c (F_0 - \tau^{-1} \rho_0^{\epsilon}) - k_1^{-} |\nabla \varphi| (\rho_0^{\epsilon} - g), \quad (C.6)$$

$$g = \rho^* (-\mathcal{E}_1 + \epsilon^{-1} \tilde{\gamma}_1 \mu), \tag{C.7}$$

where $\varphi = \varphi(\mathbf{x}, t)$ is a phase-field function that approximates the characteristic function of $\Omega_1(t)$, $\varphi^c = 1 - \varphi$ approximates the characteristic function of the substrate Ω_0 , and $\mu = B'(\varphi) - \epsilon^2 \Delta \varphi$ is the chemical potential where $B(\varphi) = 18\varphi^2(1 - \varphi)^2$ is a double well free energy. Equations (C.5) and (C.6) are solved in a large rectangular domain $\tilde{\Omega}$ that contains Ω_1 and Ω_2 . For simplicity, we do not include φ_∞ to specify that the deposition domain on the substrate is a circle and we assume that the kinetic parameters and edge energies are isotropic. The evolution of the layer is captured by the Cahn-Hilliard-like model:

$$\partial_t \varphi = |\nabla \varphi| (k_1^+ (\rho_1^\epsilon - g) + k_1^- (\rho_0^\epsilon - g)) + \frac{\beta}{\epsilon^2} \nabla \cdot (G(\phi) \nabla \mu), \tag{C.8}$$

$$\mu = B'(\varphi) - \epsilon^2 \Delta \varphi, \tag{C.9}$$

$$B(\varphi) = 18\varphi^2(1-\varphi)^2 \tag{C.10}$$

$$G(\varphi) = 2B(\varphi). \tag{C.11}$$

Below, we demonstrate using the method of matched asymptotic expansions that the DDM (C.5)–(C.11) yields a second-order accurate approximation of the sharp interface system (C.1)–(C.4). The analysis can easily be extended to the more complete model presented in the main text in section 3 where two layers are considered and the substrate geometry is circular (implemented via φ_{∞}).

C.1. Matched asymptotic expansions

Away from the layer 1 boundary $\Gamma_1(t)$, we assume that all variables are smooth and have regular expansions in ϵ , e.g.

$$\rho_i^{\epsilon} = \rho_i^{(0)} + \epsilon \rho_i^{(1)} + \epsilon^2 \rho_i^{(2)} + ..., \tag{C.12}$$

while away from Γ_1 , $\varphi = 1$ inside Ω_1 and $\varphi = 0$ outside Ω_1 to all orders. Accordingly, we see that $\rho_i^{(0)}$ satisfies equation (C.1), while the first order perturbations satisfy:

$$\partial_t \rho_i^{(1)} = D_i \Delta \rho_i^{(1)} - \tau^{-1} \rho_i^{(1)} \text{ in } \Omega_i(t).$$
 (C.13)

To provide the boundary conditions for the diffusion equations, we need to analyze the behavior of the system near Γ_i . To argue that ρ_i^{ϵ} is a second order approximation to the sharp interface solution ρ_i , we need to demonstrate that $\rho_i^{(1)} = 0$.

Near Γ_i , we introduce a stretched, local coordinate system:

$$\mathbf{x}(s, t; \epsilon) = \mathbf{X}(s, t) + \epsilon z \mathbf{n}(s, t) \tag{C.14}$$

where $\mathbf{X}(s,t)$ is a parameterization of $\Gamma_1(t)$, s is arclength, $\mathbf{n}(\mathbf{x},t)$ is the normal vector that points out of Ω_1 , $z = r(\mathbf{x},t)/\epsilon$ is a stretched normal coordinate and $r(\mathbf{x},t)$ is the signed distance from \mathbf{x} to $\Gamma_1(t)$. In the local coordinate system, derivatives become:

$$\nabla = \frac{1}{\epsilon} \mathbf{n} \partial_z + \mathbf{s} \frac{1}{1 + \epsilon z \kappa} \partial_s, \tag{C.15}$$

$$\Delta = \frac{1}{\epsilon^2} \partial_{zz} + \frac{1}{\epsilon} \frac{\kappa}{1 + \epsilon z \kappa} \partial_z + \frac{1}{1 + \epsilon z \kappa} \partial_s \left(\frac{1}{1 + \epsilon z \kappa} \partial_s \right), \tag{C.16}$$

$$\partial_t = -\frac{v_1^{\epsilon}}{\epsilon} \partial_z + \partial_t, \tag{C.17}$$

where the time derivative on the left-hand side of equation (C.17) is the full time derivative and the time derivative on the right hand side is the time partial derivative in the inner variables, and v_1^{ϵ} is the effective diffuse interface normal velocity of Γ_1 . Note that $\mathbf{n} = -\nabla \varphi/|\nabla \varphi|$. We assume that near $\Gamma_1(t)$, the inner variables can be expressed as

$$\hat{\rho}_{i}^{\epsilon}(z, s, t) = \rho_{i}^{\epsilon}(\mathbf{X}(s, t) + \epsilon z \mathbf{n}(s, t), t). \tag{C.18}$$

We assume that in the inner expansion, all variables have a regular expansion in the stretched coordinates, e.g.

$$\hat{\rho}_{i}^{\epsilon}(z, s, t) = \hat{\rho}_{i}^{(0)}(z, s, t) + \epsilon \hat{\rho}_{i}^{(1)}(z, s, t) + \epsilon^{2} \hat{\rho}_{i}^{(2)}(z, s, t) + \dots$$
 (C.19)

To match the inner and outer expansions, we assume that there is a region of overlap where both expansions are valid and must match. In particular, if we evaluate the outer solution in the inner variables, this must match the limits of the inner solutions away from the interface. That is

$$\rho_i^{\epsilon}(\mathbf{X} + \epsilon z \mathbf{n}, t) \sim \hat{\rho}_i^{\epsilon}(z, s, t), \tag{C.20}$$

as $z \to \pm \infty$ and $\epsilon \to 0$ with $\epsilon z \to 0^{\pm}$. Using the inner and outer expansions and equating the powers of ϵ , we obtain

$$\hat{\rho}_i^{(0)}(z, s, t) \sim \rho_i^{(0)}(s, t),$$
 (C.21)

$$\hat{\rho}_i^{(1)}(z, s, t) \sim \rho_i^{(1)}(s, t) + z\mathbf{n} \cdot \nabla \rho_i^{(0)}(s, t), \tag{C.22}$$

$$\hat{\rho}_{i}^{(2)}(z, s, t) \sim \rho_{i}^{(2)}(s, t) + z\mathbf{n} \cdot \nabla \rho_{i}^{(1)}(s, t) + \frac{z^{2}}{2}\mathbf{n} \cdot \nabla \nabla \rho_{i}^{(0)}(s, t) \cdot \mathbf{n},$$

$$\vdots \tag{C.23}$$

where $\rho_i^{(k)}(s, t) = \rho_i^{(k)}(\mathbf{X}(s, t), t)$.

Next, transforming the equations, plugging in the inner expansions and equating powers of ϵ we derive equations governing the inner solutions. At leading order $O(\epsilon^{-2})$, we obtain

$$\partial_z(\hat{\varphi}^{(0)}\partial_z\hat{\rho}_1^{(0)}) = 0, \tag{C.24}$$

$$\partial_z (1 - \hat{\varphi}^0) \partial_z \hat{\rho}_0^{(0)}) = 0 \tag{C.25}$$

From these equations (and the matching conditions), we conclude that

$$\partial_z \hat{\rho}_1^{(0)} = \partial_z \hat{\rho}_0^{(0)} = 0,$$
 (C.26)

so that $\hat{\rho}_0^{(0)}$ and $\hat{\rho}_1^{(0)}$ are constant in z across the inner layer. At the next order $O(\epsilon^{-1})$ we obtain:

$$-v_1^{(0)}\partial_z(\hat{\varphi}^{(0)}\hat{\rho}_1^{(0)}) = D_1\partial_z(\hat{\varphi}^{(0)}\partial_z\hat{\rho}_1^{(1)}) + k_1^+(\hat{\rho}_1^{(0)} - \hat{g}^{(0)})\partial_z\hat{\varphi}^{(0)}, \tag{C.27}$$

$$-v_1^{(0)}\partial_z(1-\hat{\varphi}^{(0)})\hat{\rho}_0^{(0)}) = D_0\partial_z(1-\hat{\varphi}^{(0)})\partial_z\hat{\rho}_0^{(1)}) + k_1^-(\hat{\rho}_0^{(0)}-\hat{g}^{(0)})\partial_z\hat{\varphi}^{(0)}. \tag{C.28}$$

Integrating these equations from $-\infty$ to ∞ in z, using that $v_1^{(0)}$ is independent of z, $\hat{\varphi}^{(0)}(+\infty) = 0$ and $\hat{\varphi}^{(0)}(+\infty) = 1$, we obtain

$$D_1 \partial_z \hat{\rho}_1^{(1)}(-\infty) + v_1^{(0)} \hat{\rho}_1^{(0)} = -k_1^+ (\hat{\rho}_1^{(0)} - \hat{g}^{(0)}), \tag{C.29}$$

$$-D_0 \partial_z \hat{\rho}_0^{(1)}(-\infty) - v_1^{(0)} \hat{\rho}_0^{(0)} = -k_1^0 (\hat{\rho}_0^{(0)} - \hat{g}^{(0)}), \tag{C.30}$$

where we have additionally used equation (C.26) and assumed that $\partial_z \hat{g}^{(0)} = 0$, a fact that will be justified later. From the matching conditions equations (C.21) and (C.22), we obtain

$$-D_1 \mathbf{n} \cdot \nabla \rho_1^{(0)} - \nu_1^{(0)} \rho_1^{(0)} = k_1^+ (\rho_1^{(0)} - g^{(0)}), \tag{C.31}$$

$$D_0 \mathbf{n} \cdot \nabla \rho_0^{(0)} + v_1^{(0)} \rho_0^{(0)} = k_1^0 (\rho_0^{(0)} - g^{(0)}), \tag{C.32}$$

where, as stated earlier, $\rho_i^{(0)}$ are the limiting values of the leading order outer solution on Ω_i and we have defined $g^{(0)} = \hat{g}^{(0)}$. Now, using that $g^{(0)} = \rho^*(-\mathcal{E}_1 - \tilde{\gamma}_1 \kappa)$, another fact we will demonstrate later, then we recover the kinetic boundary conditions equations (C.2) and (C.3). This implies that $\rho_i^{(0)}$ satisfies the sharp interface diffusion equations and kinetic boundary conditions, e.g. equations (C.1)–(C.3).

To justify the assumptions for $\hat{g}^{(0)}$ and to determine the normal velocity $v_1^{(0)}$, we need to analyze the Cahn–Hilliard-like system (C.8) and (C.9). Before doing this, however, we proceed to the next order in the inner expansion for the adatom diffusion equations in order to determine the boundary conditions for equation (C.13) for the outer solution at the next order, $\rho_i^{(1)}$. At O(1), and after manipulation, we obtain

$$-\partial_{z}(v_{1}^{(1)}\hat{\varphi}^{(0)}\hat{\rho}_{1}^{(0)} + v_{1}^{(0)}\hat{\varphi}^{(0)}\hat{\rho}_{1}^{(1)}) + \partial_{t}(\varphi^{(0)}\hat{\rho}_{1}^{(0)})$$

$$= D_{1}(\partial_{z}(\hat{\varphi}^{(0)}\partial_{z}\hat{\rho}_{1}^{(2)}) + \kappa\hat{\varphi}^{(0)}\partial_{z}\hat{\rho}_{1}^{(1)} + \hat{\varphi}^{(0)}\partial_{ss}\hat{\rho}_{1}^{(0)})$$

$$+ k_{1}^{+}(\hat{\rho}_{1}^{(1)} - \hat{g}^{(1)})\partial_{z}\hat{\varphi}^{(0)} + \hat{\varphi}^{(0)}F_{1}, \tag{C.33}$$

and

$$-\partial_{z}(v_{1}^{(1)}(1-\hat{\varphi}^{(0)})\hat{\rho}_{0}^{(0)}+v_{1}^{(0)}(1-\hat{\varphi}^{(0)})\hat{\rho}_{0}^{(1)})+\partial_{t}((1-\varphi^{(0)})\hat{\rho}_{0}^{(0)})$$

$$=D_{0}(\partial_{z}((1-\hat{\varphi}^{(0)})\partial_{z}\hat{\rho}_{0}^{(2)})+\kappa(1-\hat{\varphi}^{(0)})\partial_{z}\hat{\rho}_{0}^{(1)}+(1-\hat{\varphi}^{(0)})\partial_{ss}\hat{\rho}_{0}^{(0)})$$

$$+k_{1}^{-}(\hat{\rho}_{0}^{(1)}-\hat{g}^{(1)})\partial_{z}\hat{\varphi}^{(0)}+(1-\hat{\varphi}^{(0)})F_{0}, \tag{C.34}$$

where we have used

$$\partial_z((-v^{(0)}\hat{\rho}_1^{(0)} - D_1\partial_z\hat{\rho}_1^{(1)} - k_1^+(\hat{\rho}_1^{(0)} - \hat{g}^{(0)}))\hat{\varphi}^{(0)}) = 0, \tag{C.35}$$

$$\partial_z((-v^{(0)}\hat{\rho}_0^{(0)} - D_0\partial_z\hat{\rho}_0^{(1)} - k_1^-(\hat{\rho}_0^{(0)} - \hat{g}^{(0)}))(1 - \hat{\varphi}^{(0)})) = 0, \tag{C.36}$$

which follow from equations (C.27) and (C.28) and using the matching conditions. Next, we observe that on Γ_i :

$$-D_{i}\mathbf{n} \cdot \nabla\nabla\rho_{i}^{(0)} \cdot \mathbf{n} = D_{i}(\Delta\rho_{i}^{(0)} - \kappa\mathbf{n} \cdot \nabla\rho_{i}^{(0)} - \partial_{ss}\rho_{i}^{(0)})$$
(C.37)

$$=\partial_t \rho_i^{(0)} - F_i - D_i (\kappa \mathbf{n} \cdot \nabla \rho_i^{(0)} + \partial_{ss} \rho_i^{(0)}), \tag{C.38}$$

where we have used that $\rho_i^{(0)}$ satisfies equation (C.1). Using this in the matching conditions (C.21)–(C.23), we obtain:

$$-D_{1}\mathbf{n} \cdot \nabla \rho_{1}^{(1)} - k_{1}^{+} \rho_{1}^{(1)} - \nu^{(0)} \rho_{1}^{(1)} \sim -D_{1} \partial_{z} \hat{\rho}_{1}^{(2)} - k_{1}^{+} \hat{\rho}_{1}^{(1)} - \nu^{(0)} \hat{\rho}_{1}^{(1)} + (k_{1}^{+} + \nu^{(0)}) z \mathbf{n} \cdot \nabla \rho_{1}^{(0)} + z(\partial_{t} \rho_{1}^{(0)} - F_{1} - D_{1} (\kappa \mathbf{n} \cdot \nabla \rho_{1}^{(0)} + \partial_{ss} \rho_{1}^{(0)})).$$
(C.39)

This motivates us to rewrite equation (C.33) as

$$\begin{split} -\partial_{z}(D_{1}\hat{\varphi}^{(0)}\partial_{z}\hat{\rho}_{1}^{(2)} + v_{1}^{(1)}\hat{\varphi}^{(0)}\hat{\rho}_{1}^{(0)} + v_{1}^{(0)}\hat{\varphi}^{(0)}\hat{\rho}_{1}^{(1)}) + \partial_{t}(\hat{\varphi}^{(0)}\hat{\rho}_{1}^{(0)}) \\ -\partial_{z}(k_{1}^{+}\hat{\varphi}^{(0)}\hat{\rho}_{1}^{(1)} - z\hat{\varphi}^{(0)}(\partial_{t}\hat{\rho}_{1}^{(0)} - F_{1} + (k_{1}^{+} - D_{1}\kappa)\partial_{z}\hat{\rho}_{1}^{(1)} - D_{1}\partial_{ss}\hat{\rho}_{1}^{(0)})) \\ = D_{1}(\kappa\hat{\varphi}^{(0)}\partial_{z}\hat{\rho}_{1}^{(1)} + \hat{\varphi}^{(0)}\partial_{ss}\hat{\rho}_{1}^{(0)}) + k_{1}^{+}(\hat{\rho}_{1}^{(1)} - \hat{g}^{(1)})\partial_{z}\hat{\varphi}^{(0)} + \hat{\varphi}^{(0)}F_{1}, \\ -\partial_{z}(k_{1}^{+}\hat{\varphi}^{(0)}\hat{\rho}_{1}^{(1)} - z\hat{\varphi}^{(0)}(\partial_{t}\hat{\rho}_{1}^{(0)} - F_{1} + (k_{1}^{+} - D_{1}\kappa)\partial_{z}\hat{\rho}_{1}^{(1)} - D_{1}\partial_{ss}\hat{\rho}_{1}^{(0)})). \end{split}$$
(C.40)

where we have used that $\partial_t \rho_1^{(0)} = \partial_t \hat{\rho}_1^{(0)} - v^{(0)} \partial_z \hat{\rho}_1^{(1)}$. Next, after a series of calculations, we rewrite equation (C.40) as

$$-\partial_{z}(D_{1}\hat{\varphi}^{(0)}\partial_{z}\hat{\rho}_{1}^{(2)} + v_{1}^{(1)}\hat{\varphi}^{(0)}\hat{\rho}_{1}^{(0)} + v_{1}^{(0)}\hat{\varphi}^{(0)}\hat{\rho}_{1}^{(1)} + k_{1}^{+}\hat{\varphi}^{(0)}\hat{\rho}_{1}^{(1)} - z\hat{\varphi}^{(0)}(\partial_{t}\hat{\rho}_{1}^{(0)} - F_{1} + (k_{1}^{+} - D_{1}\kappa)\partial_{z}\hat{\rho}_{1}^{(1)} - D_{1}\partial_{ss}\hat{\rho}_{1}^{(0)}))$$

$$= -k_{1}^{+}\hat{g}^{(1)}\partial_{z}\hat{\varphi}^{(0)} + z\partial_{z}\hat{\varphi}^{(0)}(\partial_{t}\hat{\rho}_{1}^{(0)} - F_{1} + (k_{1}^{+} - D_{1}\kappa)\partial_{z}\hat{\rho}_{1}^{(1)} - D_{1}\partial_{ss}\hat{\rho}_{1}^{(0)})$$
(C.41)

where we have also assumed that $\partial_t \hat{\varphi}^{(0)} = 0$, which will be shown later. Integrating equation (C.41) in z from $-\infty$ to $+\infty$, using the matching conditions and that $\partial_z \hat{\rho}_1^{(1)}$ is independent of z from equations (C.27) and (C.29), we obtain

$$-D_1 \nabla \rho_1^{(1)} \cdot \mathbf{n} - v^{(0)} \rho_1^{(1)} = v^{(1)} \rho_1^{(0)} + k_1^+ (\rho_1^{(1)} - g^{(1)}). \tag{C.42}$$

An analogous argument can be performed to show that

$$D_0 \nabla \rho_0^{(1)} \cdot \mathbf{n} + v^{(0)} \rho_0^{(1)} = -v^{(1)} \rho_0^{(0)} + k_1^+ (\rho_0^{(1)} - g^{(1)}). \tag{C.43}$$

Assuming that $v^{(1)} = 0$ and $g^{(1)} = 0$, facts that we will prove later, we can then conclude that $\rho_1^{(1)} = \rho_0^{(1)} = 0$ since these are the unique solutions of equations (C.13) and (C.42), (C.43).

Next, we analyze the Cahn–Hilliard-like system equation (C.8)–(C.11). At the outer scale, equations (C.8), (C.9) yield 0 = 0 to all orders in ϵ because $\varphi = 0$ or 1 to all orders. The profiles of φ across Γ_1 and the normal velocity are solely determined from inner expansions. At leading order in the inner scale $O(\epsilon^{-4})$, we obtain

$$\partial_{z}(G(\hat{\varphi}^{(0)})\partial_{z}\hat{\mu}^{(0)}) = 0, \tag{C.44}$$

$$\hat{\mu}^{(0)} = B'(\hat{\varphi}^{(0)}) - \partial_{zz}\hat{\varphi}^{(0)}. \tag{C.45}$$

From the matching conditions, we conclude that

$$\hat{\mu}^{(0)} = 0,$$
 (C.46)

$$\hat{\varphi}^{(0)} = 1/2(1 - \tanh 3z). \tag{C.47}$$

Observe that $\partial_t \hat{\varphi}^{(0)} = 0$ as assumed earlier. At the next order $O(\epsilon^{-3})$, we obtain

$$\partial_{z}(G(\hat{\varphi}^{(0)})\partial_{z}\hat{\mu}^{(1)}) = 0, \tag{C.48}$$

$$\hat{\mu}^{(1)} = B''(\hat{\varphi}^{(0)})\hat{\varphi}^{(1)} - \partial_{\tau\tau}\hat{\varphi}^{(1)} - \kappa \partial_{\tau}\hat{\varphi}^{(0)}. \tag{C.49}$$

From the matching conditions, we conclude that $\partial_z \hat{\mu}^{(1)} = 0$ so that $\hat{\mu}^{(1)} = \hat{\mu}^{(1)}(s, t)$. Multiplying equation (C.49) by $\hat{\varphi}^{(0)}$ and integrating from $-\infty$ to $+\infty$ in z, we obtain

$$\hat{\mu}^{(1)}(s, t) = \kappa(s, t),$$
 (C.50)

$$\hat{\varphi}^{(1)}(s, z, t) = \frac{\kappa(s, t)}{36} (1 - \operatorname{sech}^2 3z), \tag{C.51}$$

where we have used that $\int_{-\infty}^{+\infty} (\partial_z \hat{\varphi}^{(0)})^2 dz = 1$. At the next order, $O(\epsilon^{-2})$, we obtain

$$\partial_z(G(\hat{\varphi}^{(0)})\partial_z\hat{\mu}^{(2)}) = 0, \tag{C.52}$$

$$\hat{\mu}^{(2)} = B''(\hat{\varphi}^{(0)})\hat{\varphi}^{(2)} + \frac{1}{2}B'''(\hat{\varphi}^{(0)})(\hat{\varphi}^{(1)})^2 - \partial_{zz}\hat{\varphi}^{(2)} - \kappa\partial_z\hat{\varphi}^{(1)} + z\kappa^2\partial_z\hat{\varphi}^{(0)}. \tag{C.53}$$

From the matching conditions, we also conclude that $\partial_z \hat{\mu}^{(2)} = 0$ and $\hat{\mu}^{(2)} = \hat{\mu}^{(2)}(s, t)$. Multiplying equation (C.53) by $\partial_z \hat{\varphi}^{(0)}$ and integrating from $-\infty$ to $+\infty$ in z, we obtain

$$\hat{\mu}^{(2)}(s,t) = \int_{-\infty}^{+\infty} B''(\hat{\varphi}^{(0)}) \hat{\varphi}^{(1)} \partial_z \hat{\varphi}^{(1)} dz, \tag{C.54}$$

where we have integrated by parts and used that

$$0 = \int_{-\infty}^{+\infty} \partial_z \hat{\varphi}^{(0)} \partial_z \hat{\varphi}^{(1)} dz, \tag{C.55}$$

$$0 = \int_{-\infty}^{+\infty} z(\partial_z \hat{\varphi}^{(0)})^2 \, \mathrm{d}z,\tag{C.56}$$

$$0 = \int_{-\infty}^{+\infty} (B''(\hat{\varphi}^{(0)}) - \partial_{zz}\hat{\varphi}^{(2)})\partial_z\hat{\varphi}^{(0)} dz.$$
 (C.57)

Next, from equations (C.49) and (C.50) observe that

$$B''(\hat{\varphi}^{(0)})\hat{\varphi}^{(1)}\partial_z\hat{\varphi}^{(1)} = \frac{1}{2}\partial_z(\partial_z\hat{\varphi}^{(1)})^2 + \kappa\partial_z\hat{\varphi}^{(1)}\partial_z\hat{\varphi}^{(0)} + \kappa\partial_z\hat{\varphi}^{(1)}.$$
 (C.58)

Combining equations (C.54) and (C.58), we conclude that

$$\hat{\mu}^{(2)}(s,t) = 0 \tag{C.59}$$

since $\int_{-\infty}^{+\infty} \partial_z \hat{\varphi}^{(1)} dz = 0$.

At the next order $O(\epsilon^{-1})$, we obtain

$$-v_1^{(0)}\partial_z\phi^{(0)} = \beta\partial_z(G(\phi^{(0)})\partial_z\hat{\mu}^{(3)}) + \beta G(\phi^{(0)})\partial_{ss}\hat{\mu}^{(1)} - \partial_z\phi^{(0)}(k_1^+(\hat{\rho}_1^{(0)} - \hat{g}^{(0)}) + k_1^-(\hat{\rho}_0^{(0)} - \hat{g}^{(0)})).$$
 (C.60)

Integrating equation (C.60) from $-\infty$ to $+\infty$ in z, we obtain

$$v_1^{(0)} = \beta \partial_{ss} \kappa + k_1^+ (\rho_1^{(0)} - \hat{g}^{(0)}) + k_1^- (\rho_0^{(0)} - \hat{g}^{(0)}),$$
 (C.61)

where we have used that $\hat{\mu}^{(1)} = \kappa$ from equation (C.50). Next, from equations (C.7) and (C.50) we obtain

$$\hat{g}^{(0)} = \rho^* (-\mathcal{E} + \tilde{\gamma}_1 \kappa). \tag{C.62}$$

Using these in equation (C.61), we obtain

$$v_1^{(0)} = \beta \partial_{ss} \kappa + k_1^+ (\rho_1^{(0)} - \rho^* (-\mathcal{E} + \tilde{\gamma}_1 \kappa)) + k_1^- (\rho_0^{(0)} - \rho^* (-\mathcal{E} + \tilde{\gamma}_1 \kappa)), \tag{C.63}$$

which recovers the sharp interface velocity in equation (C.4). Thus, at leading order we recover the original sharp interface system. Finally, we move to the next order O(1). Here, we obtain

$$-v_{1}^{(1)}\partial_{z}\hat{\varphi}^{(0)} - v_{1}^{(0)}\partial_{z}\hat{\varphi}^{(1)} = \beta\partial_{z}(G(\hat{\varphi}^{(0)})\partial_{z}\hat{\mu}^{(4)}) + \beta\partial_{z}(G'(\hat{\varphi}^{(0)})\hat{\varphi}^{(1)}\partial_{z}\hat{\mu}^{(3)}) + \beta\kappa G(\hat{\varphi}^{(0)})\partial_{z}\hat{\mu}^{(3)} + \beta\partial_{s}(G'(\hat{\varphi}^{(0)})\hat{\varphi}^{(1)}\partial_{s}\hat{\mu}^{(1)}) - \beta zG(\hat{\varphi}^{(0)})(\partial_{ss}\hat{\mu}^{(1)} + 3\partial_{s}\kappa\partial_{s}\hat{\mu}^{(1)}) - \partial_{z}\hat{\varphi}^{(0)}(k_{1}^{+}(\hat{\rho}_{1}^{(1)} - \hat{g}^{(1)}) + k_{1}^{-}(\hat{\rho}_{0}^{(1)} - \hat{g}^{(1)})) - \partial_{z}\hat{\varphi}^{(1)}(k_{1}^{+}(\hat{\rho}_{1}^{(0)} - \hat{g}^{(0)}) + k_{1}^{-}(\hat{\rho}_{0}^{(0)} - \hat{g}^{(0)})).$$
 (C.64)

Integrating equation (C.64) in z from $-\infty$ to $+\infty$, we obtain

$$-\int_{-\infty}^{+\infty} \partial_z \hat{\varphi}^{(0)}(v_1^{(1)} - k_1^+ \hat{\rho}_1^{(1)} - k_1^- \hat{\rho}_0^{(1)}) \, dz = \beta \kappa \int_{-\infty}^{+\infty} G(\hat{\varphi}^{(0)}) \partial_z \hat{\mu}^{(3)} \, dz, \tag{C.65}$$

where we have used that G(0) = G(1) = G'(0) = G'(1) = 0 and

$$\hat{g}^{(1)} = \rho^* \tilde{\gamma}_1 \hat{\mu}^{(2)} = 0 \tag{C.66}$$

$$0 = \int_{-\infty}^{+\infty} \partial_z \hat{\varphi}^{(1)} \, \mathrm{d}z,\tag{C.67}$$

$$0 = \int_{-\infty}^{+\infty} G'(\hat{\varphi}^{(0)}) \hat{\varphi}^{(1)} dz = \int_{-\infty}^{+\infty} G'(\hat{\varphi}^{(0)}) \partial_s \hat{\varphi}^{(1)} dz,$$

$$0 = \int_{-\infty}^{+\infty} z G(\hat{\varphi}^{(0)}) dz.$$
(C.68)

To make further progress, we observe that

$$G(\hat{\varphi}^{(0)}) = \partial_z M(\hat{\varphi}^{(0)}), \text{ where}$$
 (C.69)

$$M(\hat{\varphi}^{(0)}) = 2(\hat{\varphi}^{(0)})^3 - 3(\hat{\varphi}^{(0)})^2. \tag{C.70}$$

Using these in equation (C.60), together with the matching conditions, we obtain:

$$\beta G(\hat{\varphi}^{(0)}) \partial_z \hat{\mu}^{(3)} = \beta (M(\hat{\varphi}^{(0)}) + \hat{\varphi}^{(0)}) \partial_{ss} \kappa. \tag{C.71}$$

A direct calculation shows that

$$\int_{-\infty}^{+\infty} (M(\hat{\varphi}^{(0)}) + \hat{\varphi}^{(0)}) \, \mathrm{d}z = 0. \tag{C.72}$$

Combining this with equation (C.65) we obtain

$$0 = \int_{-\infty}^{+\infty} \partial_z \hat{\varphi}^{(0)}(v_1^{(1)} - k_1^+ \hat{\rho}_1^{(1)} - k_1^- \hat{\rho}_0^{(1)}) dz$$
 (C.73)

Next, from equations (C.35) and (C.36), and the matching conditions, we have

$$\hat{\rho}_{1}^{(1)} = \rho_{1}^{(1)}(s, t) - \frac{1}{D_{1}} z(v_{1}^{(0)} \hat{\rho}_{1}^{(0)} + k_{1}^{+} (\hat{\rho}_{1}^{(0)} - \hat{g}^{(0)})), \tag{C.74}$$

$$\hat{\rho}_0^{(1)} = \rho_0^{(1)}(s, t) - \frac{1}{D_0} z(v_1^{(0)} \hat{\rho}_0^{(0)} + k_1^- (\hat{\rho}_0^{(0)} - \hat{g}^{(0)})). \tag{C.75}$$

Using equations (C.74) and (C.75) in equation (C.73), we conclude that

$$v_1^{(1)} = k_1^+ \rho_1^{(1)}(s, t) + k_1^- \rho_0^{(1)}(s, t).$$
(C.76)

Finally, using equation (C.76) in equations (C.42) and (C.43), we obtain

$$-D_1 \nabla \rho_1^{(1)} \cdot \mathbf{n} - v^{(0)} \rho_1^{(1)} = k_1^+ \rho_1^{(1)} (1 + \rho_1^{(0)}) + k_1^- \rho_0^{(1)} \rho_1^{(0)}, \tag{C.77}$$

$$D_0 \nabla \rho_0^{(1)} \cdot \mathbf{n} + \nu^{(0)} \rho_0^{(1)} = k_1^- \rho_0^{(1)} (1 - \rho_0^{(0)}) - k_1^+ \rho_1^{(1)} \rho_0^{(0)}. \tag{C.78}$$

We can therefore conclude that $\rho_1^{(1)} = \rho_0^{(1)} = 0$, since these are the unique solutions of equations (C.13) and (C.77), (C.78), and that $v_1^{(1)} = 0$. Thus, in the region where the outer expansion is valid, we have shown

$$\rho_1^{\epsilon} = \rho_1 + O(\epsilon^2),\tag{C.79}$$

$$\rho_0^{\epsilon} = \rho_0 + O(\epsilon^2),\tag{C.80}$$

$$v_1^{\epsilon} = v_1 + O(\epsilon^2), \tag{C.81}$$

which demonstrates that the DDM (C.5)–(C.9) provides a 2nd order accurate approximation in ϵ to the sharp interface model.

Appendix D. Details of the numerical method and implementation

D.1. Numerical method

We use the Crank–Nicolson scheme to discretize the fully time-dependent system equations (13)–(25) in time on larger square domain $\tilde{\Omega}$. In particular, we let $\delta t>0$ denote the time step, and assume that ρ_0^n , ρ_1^n , ρ_0^n and μ^n are the solutions at time $t=n\delta t$. We then find the solutions at time $t=(n+1)\delta t$: ρ_0^{n+1} , ρ_1^{n+1} , ρ_0^{n+1} and μ^{n+1} by solving

$$\frac{\varphi_{\infty}H_{0}(\varphi^{n+1})\rho_{0}^{n+1} - \varphi_{\infty}H_{0}(\varphi^{n})\rho_{0}^{n}}{\delta t} = \frac{1}{2} \{ \nabla \cdot (\varphi_{\infty}H_{0}(\varphi^{n+1})D_{0}(\varphi^{n+1})\nabla\rho_{0}^{n+1}) + \varphi_{\infty}H_{0}(\varphi^{n+1})F_{0}(\varphi^{n+1}) - \varphi_{\infty}H_{0}(\varphi^{n+1})\tau_{d}^{-1}\rho_{0}^{n+1} - \varphi_{\infty}|\nabla\varphi|^{n+1}k_{0}(\varphi^{n+1})[\rho_{0}^{n+1} - \rho^{*}(\mathcal{E}(\varphi^{n+1}) + \epsilon^{-1}\gamma(\varphi^{n+1})\mu^{n+1})] \} + \frac{1}{2} \{ \nabla \cdot (\varphi_{\infty}H_{0}(\varphi^{n})D_{0}(\varphi^{n})\nabla\rho_{0}^{n}) + \varphi_{\infty}H_{0}(\varphi^{n})F_{0}(\varphi^{n}) - \varphi_{\infty}H_{0}(\varphi^{n})\tau_{d}^{-1}\rho_{0}^{n} - \varphi_{\infty}|\nabla\varphi|^{n}k_{0}(\varphi)[\rho_{0}^{n} - \rho^{*}(\mathcal{E}(\varphi^{n}) + \epsilon^{-1}\gamma(\varphi^{n})\mu^{n})] \}, \tag{D.1}$$

$$\frac{\varphi_{\infty}H_{1}(\varphi^{n+1})\rho_{1}^{n+1} - \varphi_{\infty}H_{1}(\varphi^{n})\rho_{1}^{n}}{\delta t} = \frac{1}{2} \{ \nabla \cdot (\varphi_{\infty}H_{1}(\varphi^{n+1})D_{1}\nabla\rho_{1}^{n+1}) \\
+ \varphi_{\infty}H_{1}(\varphi^{n+1})F_{1} - \varphi_{\infty}H_{1}(\varphi^{n+1})\tau_{d}^{-1}\rho_{1}^{n+1} - \varphi_{\infty}|\nabla\varphi|^{n+1}k_{1}(\varphi^{n+1})[\rho_{1}^{n+1} \\
- \rho^{*}(\mathcal{E}(\varphi^{n+1}) + \epsilon^{-1}\gamma(\varphi^{n+1})\mu^{n+1})] \} \\
+ \frac{1}{2} \{ \nabla \cdot (\varphi_{\infty}H_{1}(\varphi^{n})D_{1}\nabla\rho_{1}^{n}) + \varphi_{\infty}H_{1}(\varphi^{n})F_{1} - \varphi_{\infty}H_{1}(\varphi^{n})\tau_{d}^{-1}\rho_{1}^{n} \\
- \varphi_{\infty}|\nabla\varphi|^{n}k_{1}(\varphi^{n})[\rho_{1}^{n} - \rho^{*}(\mathcal{E}(\varphi^{n}) + \epsilon^{-1}\gamma(\varphi^{n})\mu^{n})] \}, \tag{D.2}$$

$$\frac{\varphi^{n+1} - \varphi^{n}}{\delta t} = \frac{1}{2} \{ \epsilon^{-2} \beta \nabla \cdot (B(\varphi^{n+1}) \nabla \mu^{n+1}) + \epsilon^{-1} \beta \nabla \cdot (B(\varphi^{n}) \nabla \mu^{n}) \}
+ \frac{1}{2} \{ |\nabla \varphi|^{n+1} [k_{0}(\varphi^{n+1})(\rho_{0}^{n+1} - \rho^{*}(\mathcal{E}(\varphi^{n+1}) + \epsilon^{-1} \gamma(\varphi^{n+1}) \mu^{n+1})
+ k_{1}(\varphi^{n+1})(\rho_{1}^{n+1} - \rho^{*}(\mathcal{E}(\varphi^{n+1}) + \epsilon^{-1} \gamma(\varphi^{n+1}) \mu^{n+1})] \}
+ \frac{1}{2} \{ |\nabla \varphi|^{n} [k_{0}(\varphi^{n})(\rho_{0}^{n} - \rho^{*}(\mathcal{E}(\varphi^{n}) + \epsilon^{-1} \gamma(\varphi^{n}) \mu^{n})
+ k_{1}(\varphi^{n})(\rho_{1}^{n} - \rho^{*}(\mathcal{E}(\varphi^{n}) + \epsilon^{-1} \gamma(\varphi^{n}) \mu^{n})] \},$$
(D.3)

$$\mu^{n+1} = -\epsilon^2 \Delta \varphi^{n+1} + G'(\varphi^{n+1}), \tag{D.4}$$

with the following boundary conditions

$$\nabla \rho_0^{n+1} \cdot \mathbf{n} = \nabla \rho_1^{n+1} \cdot \mathbf{n} = \nabla \varphi^{n+1} \cdot \mathbf{n} = \nabla \mu^{n+1} \cdot \mathbf{n} = 0$$
 on $\partial \tilde{\Omega}$. (D.5)

Moreover, we add a small positive parameter $\delta = 10^{-5}$ to the functions H_0 , H_1 and $B(\varphi)$ in all second-order differential operators in (D.1)–(D.4) as a regularization.

D.2. Implementation

Standard, cell-centered central-difference finite difference methods are used, together with a block-structured adaptive mesh, to discretize the equations in space. The nonlinear equations at the implicit time level are solved using an efficient nonlinear FAS multigrid solver. See [25] for details. Here, we use a four-level block-structured adaptive mesh, which consists of one root level (grid size h_0) and three refinement levels (grid size h_i) with refinement ratio of 2. For each adaptive mesh level, we refine the grid cell (i, j) wherever $h_i | \nabla \varphi_{i,j} | > q_{tol}$. Here, we set $q_{tol} = 0.01$.

Appendix E. Convergence of anisotropic layer dynamics

Here we present the convergence analysis using the fully time-dependent dynamics. The results for quasi-steady dynamics are similar (not shown). Using the parameters in section 4.3, we analyze the

Table E1. Convergence test for adatom concentrations ρ_2 , ρ_1 and ρ_0 using six-fold symmetric anisotropic edge energies and kinetic coefficients in section 4.3.

t = 0.1	ℓ_2					
ϵ	$E^{(2)}_{\epsilon_{i-1},\epsilon_i, ho_2}$	Rate	$E^{(2)}_{\epsilon_{i-1},\epsilon_i, ho_1}$	Rate	$E^{(2)}_{\epsilon_{i-1},\epsilon_i, ho_0}$	Rate
0.4	1.172×10^{-3}	_	1.642×10^{-3}		1.007×10^{-3}	
0.2	1.143×10^{-3}	0.04	1.454×10^{-3}	0.18	1.065×10^{-3}	-0.08
0.1	6.485×10^{-4}	0.82	8.359×10^{-4}	0.80	7.196×10^{-4}	0.57
0.05	1.942×10^{-4}	1.74	2.631×10^{-4}	1.67	2.734×10^{-4}	1.40
0.025	5.304×10^{-5}	1.87	6.413×10^{-5}	2.04	7.654×10^{-5}	1.84
t = 0.1	ℓ_{∞}					
$\overline{\epsilon}$	$E_{\epsilon_{i-1},\epsilon_{i}, ho_{2}}^{(\infty)}$	Rate	$E^{(\infty)}_{\epsilon_{i-1},\epsilon_i, ho_1}$	Rate	$E^{(\infty)}_{\epsilon_{i-1},\epsilon_i, ho_0}$	Rate
0.4	2.255×10^{-3}	_	3.240×10^{-3}	_	4.006×10^{-3}	
0.2	3.491×10^{-3}	-0.63	4.574×10^{-3}	-0.50	5.693×10^{-3}	-0.50
0.1	2.345×10^{-3}	0.57	3.233×10^{-3}	0.50	4.758×10^{-3}	0.26
0.05	7.939×10^{-4}	1.56	1.413×10^{-3}	1.19	1.848×10^{-3}	1.36
0.025	1.823×10^{-3}	2.12	4.094×10^{-4}	1.79	5.537×10^{-4}	1.74

Table E2. Convergence test for adatom concentrations ρ_2 , ρ_1 and ρ_0 using three-fold symmetric anisotropic edge energies and kinetic coefficients in section 4.3.

t = 0.1	ℓ_2					
ϵ	$E_{\epsilon i-1}^{(2)}, \epsilon_i, \rho_2$	Rate	$E^{(2)}_{\epsilon_{i-1},\epsilon_i, ho_1}$	Rate	$E^{(2)}_{\epsilon_{i-1},\epsilon_i, ho_0}$	Rate
0.4	1.584×10^{-3}	_	2.700×10^{-3}	_	1.872×10^{-3}	
0.2	1.752×10^{-3}	-0.15	2.253×10^{-3}	0.26	1.685×10^{-3}	0.15
0.1	1.016×10^{-3}	0.79	1.031×10^{-3}	1.13	7.835×10^{-4}	1.10
0.05	3.223×10^{-4}	1.66	2.789×10^{-4}	1.89	1.872×10^{-4}	2.07
0.025	8.852×10^{-5}	1.86	7.001×10^{-5}	1.99	4.502×10^{-5}	2.06
$\overline{t=0.1}$	ℓ_{∞}					
ϵ	$E^{(\infty)}_{\epsilon_{i-1},\epsilon_i, ho_2}$	Rate	$E^{(\infty)}_{\epsilon_{i-1},\epsilon_i, ho_1}$	Rate	$E^{(\infty)}_{\epsilon_{i-1},\epsilon_i, ho_0}$	Rate
0.4	7.321×10^{-3}	_	5.747×10^{-3}	_	4.228×10^{-3}	
0.2	1.001×10^{-2}	-0.45	6.091×10^{-3}	-0.08	4.982×10^{-3}	-0.24
0.1	5.620×10^{-3}	0.83	4.623×10^{-3}	0.40	2.686×10^{-3}	0.89
0.05	1.934×10^{-3}	1.54	1.940×10^{-3}	1.25	7.734×10^{-4}	1.80
0.025	5.500×10^{-4}	1.82	5.590×10^{-4}	1.80	1.931×10^{-4}	2.00

convergence of our schemes at time t=0.1. The consecutive errors (e.g. equation (30)) and convergence rates for the adatom concentrations are given in tables E1 and E2 for six-fold and three-fold symmetric anisotropic edge energies and kinetic coefficients, respectively. The results suggest the scheme is second-order convergent in both the ℓ_2 and ℓ_∞ norms.

ORCID iDs

Zhenlin Guo https://orcid.org/0000-0003-3219-6418

References

- [1] Choi J H, Cui P, Chen W, Cho J H and Zhang Z Y 2017 Atomistic mechanisms of van der waals epitaxy and property optimization of layered materials *Wiley Interdiscip. Rev.-Comput. Mol. Sci.* 7 e1300
- [2] Duong D L, Yun S J and Lee Y H 2017 van der waals layered materials: opportunities and challenges ACS Nano 11 11803–30
- [3] Gobbi M, Orgiu E and Samori P 2018 When 2d materials meet molecules: opportunities and challenges of hybrod organic/inorganic van der waals heterostructures Adv. Mater. 30 1706103
- [4] Hong H, Liu C, Cao T, Jun C H, Wang S X, Wang F and Liu K H 2017 Interfacial engineering of van der waals coupled 2d layered materials *Adv. Mater. Interfaces* 4 1601054
- [5] Shi Z, Wang X, Sun Y H, Li Y W and Zhang L J 2018 Interlayer coupling in two-dimensional semiconductor materials Semicond. Sci. Technol. 33 093001
- [6] Frisenda R, Navarro-Moratalla E, Gant P, De Lara D P, Jarillo-Herrero P, Gorbachev R V and Castellanos-Gomez A 2018 Recent progress in the assembly of nanodevices and van der waals heterostructures by deterministic placement of 2d materials *Chem. Soc. Rev.* 47 53–68
- [7] Solis-Fernandez P, Bissett M and Ago H 2017 Synthesis, structure and applications of graphene-based 2d heterostructures Chem. Soc. Rev. 46 4572–613
- [8] Gong Y G et al 2014 Vertical and in-plane heterostructures from WS₂/MOS₂ monolayers Nat. Mater. 13 1135–42
- [9] Gong Y J et al 2015 Two-step growth of two-dimensional WSe₂/MOSe₂ heterostructures Nano Lett. 15 6135–41
- [10] Lu C-C, Lin Y-C, Yeh C-H, Suenaga K and Chiu P-W 2013 Twisting bilayer graphene superlattices ACS Nano 7 2587–94
- [11] Xia M, Yin K B, Capellini G, Niu G, Gong Y J, Zhou W, Ajayan P M and He Y H 2015 Spectroscopic signatures of aa' and ab stacking of chemical vapor deposited bilayer MOS₂ ACS Nano 9 12246–54
- [12] Chen W, Cui P, Zhu W G, Kaxiras E, Gao Y F and Zhang Z Y 2015 Atomistic mechanisms for bilayer growth of graphene on metal substrates *Phys. Rev.* B 91 045408
- [13] Zhang X Y, Wang L, Xin J, Yakobson B I and Ding F 2014 Role of hydrogen in graphene chemical vapor deposition growth on a copper surface J. Am. Chem. Soc. 136 3040–7
- [14] Ye H, Zhou J D, Er D Q, Price C C, Yu Z Y, Liu Y M, Lowengrub J S, Lou J, Liu Z and Shenoy V B 2017 Toward a mechanistic understanding of vertical growth of van der waals stacked 2d materials: a multiscale model and experiments *ACS Nano* 11 12780–8
- [15] Burton W K, Cabrera N and Frank F C 1951 The growth of crystals and the equilibrium structure of their surfaces Proc. R. Soc. A 243 299–358
- [16] Kockelkoren J, Levine H and Rappel W-J 2003 Computational approach for modeling intra- and computational approach for modeling intra- and extracellular dynamics *Phys. Rev.* E 68 037702
- [17] Li X, Lowengrub J, Ratz A and Voigt A 2009 Solving pdes in complex geometries: a diffuse domain approach Commun. Math. Sci. 7 81–107
- [18] Teigen K E, Li X, Lowengrub J, Wang F and Voigt A 2009 A diffuse-interface approach for modeling transport, diffusion and adsorption/desorption of material quantities on a deformable interface Commun. Math. Sci. 7 1009–37
- [19] Yu Y C, Chen H Y and Thornton K 2012 Extended smoothed boundary method for solving partial differential equations with general boundary conditions on complex boundaries *Modelling Simul. Mater. Sci. Eng.* 20 075008
- [20] Poulsen S O and Voorhees P W 2018 Smoothed boundary method for diffusion-related partial differential equations in complex geometries Int. J. Comput. Methods 15 1850014
- [21] Lervåg K Y and Lowengrub J 2015 Analysis of the diffuse-domain method for solving PDEs in complex geometries Commun. Math. Sci. 13 1473–500
- [22] Burger M, Elvetun O L and Schlottbom M 2017 Analysis of the diffuse domain method for second order elliptic boundary value problems *Found. Comput. Math.* 17 627–74
- [23] Rätz A 2015 A new diffuse-interface model for step flow in epitaxial growth *IMA J. Appl. Math.*
- [24] Meca E, Shenoy V B and Lowengrub J 2017 H 2 -dependent attachment kinetics and shape evolution in chemical vapor deposition graphene growth 2D Mater. 4 031010

- [25] Feng W, Guo Z, Lowengrub J S and Wise S M 2018 A mass-conservative adaptive FAS multigrid solver for cell-centered finite difference methods on block-structured, locally-cartesian grids *J. Comput. Phys.* **352** 463–97
- [26] Rajan A G, Warner J H, Blakschtein D and Strano M S 2016 Generalized mechanistic model for the chemical vapor deposition of 2d transition metal dichalcogenide monolayers ACS Nano 10 4330-44